nature communications

Article

https://doi.org/10.1038/s41467-024-51600-6

Mechanistic insights into lanthipeptide modification by a distinct subclass of LanKC enzyme that forms dimers

Received: 5 December 2023

Accepted: 13 August 2024

Published online: 17 August 2024

Check for updates

Yifan Li[1,4], Kai Shao[1,4], Zhaoxing Li[2,4], Kongfu Zhu[1], Bee Koon Gan[1], Jian Shi[3], Yibei Xiao[2] & Min Luo[1,3]

Naturally occurring lanthipeptides, peptides post-translationally modified by various enzymes, hold significant promise as antibiotics. Despite extensive biochemical and structural studies, the events preceding peptide modification remain poorly understood. Here, we identify a distinct subclass of lanthionine synthetase KC (LanKC) enzymes with distinct structural and functional characteristics. We show that PneKC, a member of this subclass, forms a dimer and possesses GTPase activity. Through three cryo-EM structures of PneKC, we illustrate different stages of peptide PneA binding, from initial recognition to full binding. Our structures show the kinase domain complexed with the PneA core peptide and GTPγS, a phosphate-bound lyase domain, and an unconventional cyclase domain. The leader peptide of PneA interact with a gate loop, transitioning from an extended to a helical conformation. We identify a dimerization hot spot and propose a "negative cooperativity" mechanism toggling the enzyme between tense and relaxed conformation. Additionally, we identify an important salt bridge in the cyclase domain, differing from those in in conventional cyclase domains. These residues are highly conserved in the LanKC subclass and are part of two signature motifs. These results unveil potential differences in lanthipeptide modification enzymes assembly and deepen our understanding of allostery in these multifunctional enzymes.

Lanthipeptides, widely found in nature, offer a promising alternative to traditional drugs that can foster antimicrobial resistance[1–5]. These peptides play a crucial role in the innate immunity of various organisms, including humans (e.g., defensins and cathelicidin)[6–8]. In addition to their physiological functions, characterization of lanthipeptides revealed a variety of medically interesting bioactivities[5,9,10].

Biosynthesis of lanthipeptides is a mostly conserved process in gram-positive bacteria[11–15]. Typically, the bacterial genome encodes both a precursor peptide, LanA, and a biosynthetic enzyme that modifies it. The precursor peptide consists of an N-terminal leader peptide (LP) responsible for substrate recognition and a C-terminal core peptide (CP) that will be bound and modified by the modification enzyme[16]. The modified CP will then be cleaved off from the LP to yield the mature lanthipeptide with antimicrobial activity[17] (Supplementary Fig. 1a). Modification of LanA by lanthipeptide synthetases occurs in three main steps (Supplementary Fig. 1b). Initially, a Ser or Thr residue in the precursor peptide is activated by either glutamylation or phosphorylation, which allows for subsequent β-elimination that yields either dehydroalanine (Dha) or dehydrobutyrine (Dhb). Finally, a stereoselective Michael-type addition occurs, in which an adjacent cysteine thiol engages with the β-position of Dha or Dhb, resulting in the formation of a thioether

[1]Department of Biological sciences, Faculty of Science, National University of Singapore, Singapore, Singapore. [2]Department of Pharmacology, School of Pharmacy, China Pharmaceutical University, Nanjing, China. [3]Center for Bioimaging Sciences, Department of Biological Sciences, National University of Singapore, Singapore, Singapore. [4]These authors contributed equally: Yifan Li, Kai Shao, Zhaoxing Li. e-mail: dbslmin@nus.edu.sg

linkage. In certain lanthipeptides, further modifications can occur, such as labionin formation upon dehydration and macrocyclization of the SxxSxxxC motif of the CP (citation)[11,12,18]. Lanthipeptides are categorized into five classes based on the structure of their modification enzymes[15,19,20] (Supplementary Fig. 1b). In Class I, lanthipeptides are modified by two monofunctional enzymes, LanB and LanC[21–23]. In Class II, lanthipeptides are modified by the bifunctional enzyme LanM, which contains both a dehydratase and a cyclase domain[24,25]. In the recently discovered Class III and Class IV, lanthipeptides are modified by LanKC and LanL, respectively, enzymes that contain lyase, kinase, and cyclase domains[26,27]. In Class V, the three lanthipeptide-modifying activities are encoded in individual polypeptides[28,29]. Distinct from all other classes, the modification enzymes of Class III lanthipeptides contain an unconventional cyclase domain, which is distinct in that it lacks the catalytic residues conserved in conventional cyclases and carries out cyclization without relying on Zn^{2+} [30,31].

Previous structural investigations have significantly advanced our understanding of the structure and catalytic mechanisms of modification enzymes in Class I, Class II, Class III and Class IV[21,23,24,26]. Structures have been determined for the kinase domain of the Class III modification enzyme CurKC[32] and more recently for the Class IV enzyme from *Thermomonospora curvata*, CuvL, both in the presence and absence of bound peptide substrate[26]. Additionally, the structure of a full-length ThurKC, a Class III LanKC enzyme from *Bacillus thuringiensis*, has been reported[33], also in the presence and absence of bound peptide substrate, accompanied by elegant biochemical studies (Fig. 1a). These long-sought structures for Class III and IV enzymes provided detailed information for peptide recognition. The ThurKC structure, in particular, offered information on the catalytic

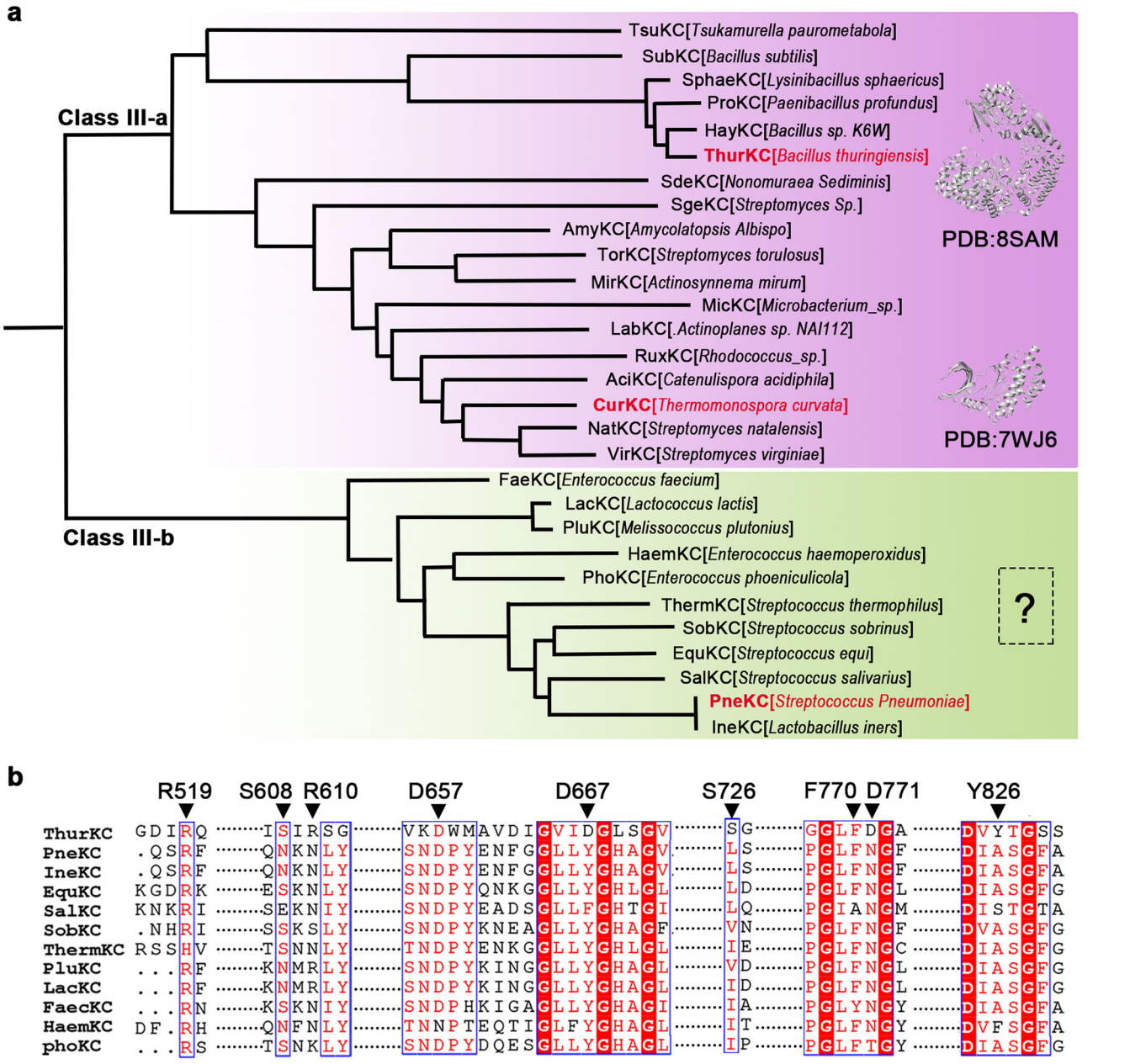

Fig. 1 | Sequence analysis reveals two distinct groups of Class III lanthipeptide modification enzymes. a Maximum likelihood phylogeny of Class III lanthipeptide modification enzymes identifies two prominent subclasses, referred to as Class III-a (purple) and Class III-b (green). **b** Sequence alignment of the cyclase domain from Class III-a enzyme ThurKC and Class III-b enzyme LanKCs. The residues found to be crucial for cyclase domain activity in Class III-a ThurKC are largely absent in Class III-b LanKCs.

residues in the noncanonical cyclase domain that is distinct to Class III enzymes. However, a previous study revealed extensive variations among Class III LanKC enzymes[34], warranting further structural and functional studies.

All bifunctional and trifunctional modification enzymes characterized to date, including LanKC[24,26,27], exist as monomers, but Class I enzyme NisB was found to form dimers[21]. This finding hints at a potential divergence in the overall assembly of these enzymes, establishing the need for further investigation into whether some enzymes from other classes may also form dimers and into the evolutionary significance and mechanistic purpose of dimerization. In addition, our understanding of lanthipeptide modification enzymes is predominantly based on structures determined by X-ray crystallography, and work is thus still needed to fully appreciate the dynamic processes involved in peptide recognition and domain coordination within these multifunctional enzymes. The absence of peptides bound at catalytic sites has further limited our understanding of how intermediates are shuttled between different domains during the modification process. In conclusion, further research is needed to obtain a more comprehensive understanding of the intricate mechanisms at play in lanthipeptide modification enzymes.

In this study, we characterized a distinct subgroup of Class III LanKC enzymes, which we termed Class III-b, that features a distinct cyclase domain sequence. A detailed structure-function analysis of PneKC, a Class III-b LanKC from *Streptococcus pneumoniae*, revealed that it forms a dimer and has GTPase activity. Three cryo-EM structures showed a tripartite complex in which the kinase domain binds to both the CP of its substrate peptide, PneA, and GTPγS, identifying a potential recognition motif for peptide binding to the kinase domain. Additionally, we resolved a bipartite complex, with the lyase domain interacting with a product phosphate and the cyclase domain featuring two catalytic residues, that are part of two of the three signature motifs we found to be distinct to this subclass. Furthermore, our study provides a glimpse into the dynamic behavior of the substrate peptide during the recognition process, revealing a transition of the LP from an extended to a helical conformation. The helical conformation only emerges upon full binding of the LP, when its N-terminus is locked underneath the gate loop of the kinase domain, which is located at a position that is distinct from that observed in Class IV CuvL. We also uncovered a hot spot for dimerization within the enzyme and proposed a negative cooperativity mechanism that governs transitions between a tense and a relaxed conformation, significantly impacting enzyme activity. Our findings contribute to a broader understanding of lanthipeptide modification enzymes and their regulatory mechanisms.

Results

Class III LanKC enzymes fall into two groups with distinct cyclase domains

To unravel the intricacies of Class III LanKC enzymes and to identify potential catalytic residues in their noncanonical cyclase domain, we first performed a sequence analysis. Interestingly, our bioinformatic investigation revealed that Class III LanKCs fall into two major classes that we designated as Class III-a and Class III-b (Fig. 1a) (Supplementary Data 1). The sequence identity between members of these two subclasses is less than 26%. Notably, while the lyase and kinase domains are highly conserved in the two subclasses, the cyclase domains diverge substantially (Supplementary Fig. 2a). A recent study of ThurKC[33], which falls into Class III-a, identified several catalytic residues in its cyclase domain. However, many of these residues are absent in the recently identified Class III-b enzymes (Fig. 1b).

Within the Class III-b LanKC subgroup, we observed several conserved motifs in the cyclase domain that were previously not identified in lanthipeptide modification enzymes (Supplementary Fig. 2b, top panel). Three highly conserved signature motifs stand out in the cyclase domain: a FPVHYYG motif close to the N-terminus, a QxxQxxRxLPY motif near the middle, and a GxxxAGDxG motif close to the C-terminus (Supplementary Fig. 2b). Importantly, these motifs are absent in members of other LanKC classes, in particular in Class III-a LanKCs (Supplementary Fig. 2b, bottom panel). We therefore propose these motifs to be signatures for Class III-b LanKCs. Our observation also implies that while the cyclase domain in Class III-a and Class III-b LanKCs have the same function, they appear to use different mechanisms.

Furthermore, analysis of the precursor peptide LanA from Class III-b systems showed that these share several conserved features (Supplementary Fig. 2c), including several charged residues and a conserved θxxθxxθ motif within the LP (residues 5–8 in Class III-b LanA peptides)[34] and two tandem SxxSxxxC motifs in the variable CP region that are also present in many other LanKC enzymes[35]. Notably, many Class III-b LanA peptides have a bulky aromatic residue, such as Phe or Tyr, in the position before the first Ser residue in the SxxSxxxC motif (Supplementary Fig. 2c).

PneKC forms a dimer with obvious GTPase activity in the presence of PneA

To facilitate our structure-function analysis of Class III-b lanthipeptide modification enzymes, we screened multiple Class III-b enzymes and decided to work on the LanKC enzyme from *Streptococcus pneumoniae* (Pne) (ATCC BAA-255D-5) due to its high expression level and stability. The putative biosynthetic gene cluster of the lanthipeptide PneA is arranged in a series of components. A central region encodes a putative heterodimeric ABC transporter for peptide secretion, an S9 peptidase, likely involved in LP removal, the modification enzyme PneKC, and the PneA precursor peptide (Supplementary Fig. 3a). An upstream region encodes another PneA precursor, differing by a single amino acid, followed by a permease protein, which has been reported in other classes but remains poorly studied[36–38]. A downstream region encodes an intramembrane metalloprotease (IMMP) whose function in lanthipeptide biosynthesis remains unknown. For our study, we cloned and expressed PneKC, together with its peptide substrate, PneA, in *E. coli* BL21(DE3). Details are described in the "Methods" section, and the primers used for cloning are listed in Supplementary Table 1. Unmodified PneA showed limited solubility. For purification, we therefore denatured PneA by adding urea, which we then removed by dialysis (Supplementary Fig. 3b). In an alternative approach, we obtained stable PneA by co-expressing it with PneKC using the PQlink vector (Supplementary Fig. 3b).

Our size-exclusion chromatography (SEC) profiles indicated that PneKC purified as a dimer, regardless of the presence of PneA (Fig. 2a). This conclusion was based on comparison with a protein standard curve that was generated by SEC runs of proteins with known molecular weight (Supplementary Fig. 3c), but was further supported by negative-stain EM results. 2D-class averages of PneKC showed particles with a diameter of ~12 nm and two distinct lobes, indicative of a dimeric structure (Supplementary Fig. 3e). We believe that PneKC is the earliest documented dimer among multifunctional lanthipeptide modification enzymes, indicating unexplored differences in the assembly and oligomeric state of LanKC enzymes.

Previous studies revealed that different LanKC enzymes utilize different nucleotides. For instance, LabKC strictly requires GTP[39], whereas EryKC and MicKC exclusively utilize ATP[40,41]. Other LanKCs, such as AciKC, have no discernible preferences and can utilize various NTPs[30]. We thus examined the nucleotide preference of PneKC and its relationship with peptide binding. For PneKC by itself, the basal nucleotide hydrolysis activity was quite low. Even at a high enzyme concentration (5 mg/ml), hydrolysis was barely observed for different nucleotide triphosphates (NTPs), including ATP, GTP, CTP, UTP, and TTP (Fig. 2b). However, addition of PneA (at an equal molar amount as PneKC monomer) significantly increased the nucleotide hydrolysis

https://doi.org/10.1038/s41467-024-51600-6

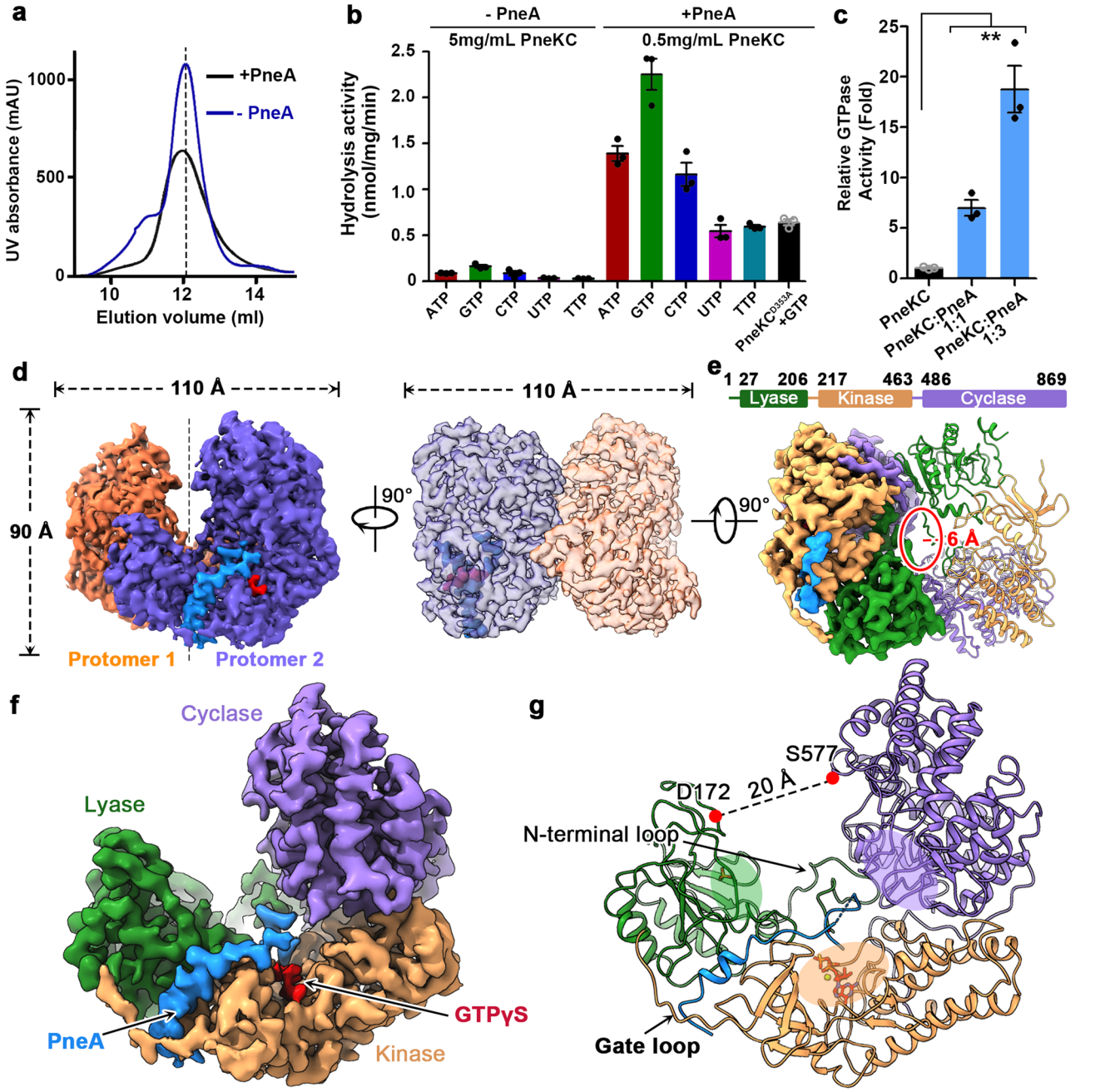

Fig. 2 | Biochemical and cryo-EM analyzes show that PneKC forms a dimer. a The size-exclusion chromatography (SEC) profiles of PneKC alone (blue) and in complex with PneA (black) show distinct peaks at 12.1 ml and 12.2 ml, respectively, corresponding to a mass of approximately 200 kDa, indicating that PneKC by itself likely forms a dimer. **b** Nucleotide hydrolysis of PneKC was assayed using various nucleotides as substrates, both in the absence of PneA as well as in the presence of PneA at a PneKC monomer to PneA ratio of 1:1. Catalytic residue Asp353 in the kinase domain was initially mutated to alanine as a negative control as it was expected to abolish nucleotide hydrolysis. However, this mutant displayed noticeable activity even in the absence of PneA. PneKC (5 mg/ml) with different NTPs in the absence of PneA, exhibited very low hydrolysis activity. However, in the presence of PneA, significant hydrolysis activity was observed with various NTPs, even at a much lower PneKC concentration of 0.5 mg/ml. Error bars represent the standard deviation (SD) of three independent experiments ($n = 3$). **c** GTPase activity of PneKC with different amounts of PneA. Error bars represent the standard deviation (SD) ($n = 3$), and the statistical significance was assessed using a two-tailed t-test ($n = 3$) where PneKC: PneA (1:1) $p = 0.0037$; PneKC: PneA (1:3) $p = 0.004$. The indicated ratio is for PneKC monomer to PneA. **d** Top and side views of the density map of the PneKC-PneA complex showing the two PneKC protomers (ligand-bound protomer: purple; ligand-free protomer: orange; bound PneA: blue; and GTPγS: red). The two protomers are arranged in a head-to-tail manner. **e** Model of dimeric PneKC showing the N-terminal lyase domain (green), the central kinase domain (sandy brown), and the C-terminal putative cyclase domain (purple). **f** The PneKC protomer forms a cashew shape with PneA bound to the major groove that is formed between the lyase and kinase domains. **g** Model of PneKC showing an expansive central groove. The catalytic sites of the three domains are oriented towards the central cavity. Source data are provided as a Source Data file.

activity for all tested NTPs, with the highest activity measured for GTP (Fig. 2b). Our Michaelis-Menten kinetics analysis of PneKC revealed a higher binding affinity of 0.14 mM for GTP as compared to 0.25 mM for ATP, as well as a higher Kcat value of 0.58 s^{-1} for GTP as compared to 0.35 s^{-1} for ATP (Supplementary Fig. 3d). In addition, we also studied the D353A mutant as negative control. Mutation of this catalytic residue in the kinase domain completely abolished phosphorylation activity in CuvL[26]. Although this mutant showed some activity in the

presence of PneA (Fig. 2b), its activity was much lower than that of WT PneKC, confirming the observed nucleotide hydrolysis activity of WT PneKC. To further check the effect of PneA on GTPase activity, we assessed the hydrolysis activity of PneKC in the presence of varying amounts of PneA. At a molar PneKC monomer to PneA ratio of 1:1, there was a 7-fold increase in GTP hydrolysis activity, which further increased to 18-fold when the molar ratio was increased to 1:3 (Fig. 2c). Together, these results demonstrate that our purified PneKC is active and can utilize multiple nucleotides as substrates, with a preference for GTP.

We found that cleavage of the His tag caused PneKC to aggregate, presumably due to partial denaturation. Therefore, all PneKC enzymes used in this study had an N-terminal His tag. To confirm that the His tag does not interfere with the function of PneKC, we generated a construct with PneKC and PneA under the same operon, in which only PneA, but not PneKC, had an N-terminal His tag. Following purification, the complex of PneA with untagged PneKC served as a control for comparison with the tagged version (Supplementary Fig. 3b). Both PneKC variants, with and without His tag, formed dimers as seen by SDS-PAGE and negative-stain EM imaging (Supplementary Fig. 3e). Further, at the same PneA level, as confirmed by SDS-PAGE (Supplementary Fig. 3b), both untagged and His-tagged PneKC complexes showed similar GTPase activity (Supplementary Fig. 3f). We also assessed the effect of a His tag on PneA. For this purpose, we measured the Michaelis-Menten kinetics of PneKC in the presence of untagged PneA. When we measured the GTPase activity of PneKC in the presence of untagged PneA (Supplementary Fig. 3d) under the same conditions we used with His-tagged PneA (Supplementary Fig. 3f), we found no significant difference. Specifically, when we set the molar PneKC monomer to PneA ratio to 1, we measured the same GTPase activity. Collectively, these findings demonstrate that the presence of a His tag neither on PneKC nor on PneA interferes with the structural integrity or function of the purified proteins.

To directly confirm the peptide modification activity of purified PneKC, we conducted an experiment in which we incubated N-terminally His-tagged precursor PneA (HHHHHHHGAAGTSLYKKAGENLYFQG-PneA) with PneKC in the presence of 1 mM GTP/Mg^{2+} and 5 mM TCEP for 1 h at 37 °C. As a control, we subjected PneA to the same incubation but without PneKC. Both samples were then analyzed by intact mass spectrometry (MS) (Supplementary Fig. 3g, upper). The intact mass of the PneA product in the absence of PneKC was 8321.5 Da, which is 1.6 Da lower than the theoretical mass of precursor PneA of 8323.1 Da. The intact mass of the modified PneA product was 8232.8 Da, consistent with the removal of five water molecules from the precursor. These findings suggest that PneKC is fully active in modifying PneA.

To further validate these results, we employed free cysteine thiol labeling using S-methyl methanethiosulfonate (MMTS) for subsequent MS analysis[42]. In this approach, cysteines in unmodified PneA should become labeled with MMTS, whereas the cysteines in fully modified PneA would be cyclized and could thus not be labeled with MMTS. Indeed, our results demonstrated that the PneA product after incubation with PneKC exhibited no mass shift after addition of MMTS, indicating no MMTS labeling. Conversely, PneA incubated without PneKC displayed a clear mass shift of 93.7 Da after the addition of MMTS, which is consistent with the addition of two MSH [+45.98 Da] conjugations (Supplementary Fig. 3g, bottom). These results confirm the ability of N-terminal His-tagged PneKC to modify PneA and suggest that both SxxSxxxC motifs in the CP were modified.

In summary, we were able to purify recombinant PneKC and found that it forms a dimer and can utilize multiple NTPs as substrates, with a preference for GTP. In addition, MS experiments confirmed that purified PneKC can modify PneA, cyclizing both SxxSxxxC motifs in the CP.

The dimer structure formed by class III-b LanKC

We used single-particle cryo-EM to determine the structure of a PneKC-PneA complex that was purified in the presence of 1 mM $MgCl_2$ and GTPγS (Supplementary Fig. 4). The purified complex exhibited a molar PneKC monomer to PneA ratio of close to 0.5 (Supplementary Fig. 3b), suggesting that PneA bound to only approximately half of the PneKC molecules. This finding was supported by our cryo-EM analysis, which yielded a 3.7-Å resolution density map (Supplementary Fig. 4b). The map allowed us to model all three domains and revealed that PneA and nucleotide bound predominantly to just one PneKC protomer (Supplementary Fig. 4 and 5).

PneKC has a homodimeric architecture that is distinct from those of all previously studied lanthipeptide modification enzymes (Fig. 2e). The overall structure of PneKC has two-fold symmetry and the dimensions are 125 Å in length and width, and 105 Å in height. The two monomers interact closely in a head-to-tail configuration (Fig. 2f), resulting in a tight dimer that encompasses a small hole (radius of 6 Å) along its two-fold symmetry axis (Fig. 2f). Each protomer acts as a stabilizing scaffold for its counterpart, potentially enhancing the overall stability of the enzyme. Interestingly, AlphaFold-Multimer[43] also predicted a dimer and the predicted dimer closely resembled our experimental structure, with only minor local variations in sidechain conformations at the dimer interface and a different angle between the cyclase and lyase domains within each protomer (Supplementary Fig. 6). This result highlights the potential of AlphaFold-Multimer in predicting complexes formed by lanthipeptide modification enzymes.

Class III LanKC, as Class IV enzymes, is characterized by three catalytic domains (Fig. 2g): an N-terminal lyase domain, a central kinase domain, and a large C-terminal cyclase domain. The cyclase domain shares low sequence similarity to traditional cyclase domains (16.3% with the cyclase domain of Class IV CuvL, 21.4% with Class II LanM2, and 6.7% with Class I NisC). Moreover, the absence of conserved key residues leaves the mechanism elusive. Within each protomer, the lyase and cyclase domains are at opposite ends and separated by a distance of over 20 Å (measured as the distance between residues Asp172 and Ser577) (Fig. 2h). The kinase domain bridges the two distal domains. The expansive internal groove is an ideal location for sequential peptide modification, in particular, because all three catalytic sites are oriented towards this internal groove (Fig. 2h).

The conformation of the individual PneKC protomers differs from those of the two previously reported trifunctional enzymes, ThurKC and CuvL[26,27] (Supplementary Fig. 7a). The root-mean-square deviation (RMSD) between PneKC and the Class III-a enzyme ThurKC is 7.24 Å over 800 residues. There are distinct structural differences in the β6L loop, a partially unwound β-bow tie motif initially described for CuvL[26], and in the N-terminal region. ThurKC features an α helix in the N-terminal region formed by residues Gly3 to Leu11. There is also a substantial difference in the distance between the cyclase and lyase domains. In ThurKC, the β-bow tie extends towards the cyclase domain, creating a compact central catalytic groove that measures just 11.7 Å (the distance between residues His174 and Asp650). By contrast, PneKC has a broader groove that spans 20 Å at its narrowest point (between residues Asp172 and Ser577). PneKC is also very different from the Class IV enzyme CuvL. In CuvL, the β-bow tie structure extends directly into the cyclase domain, resulting in an overall closed, ring-like structure.

The structure of the kinase domain with bound core peptide and GTPγS reveals a potential motif for peptide recognition

PneA is first phosphorylated by the kinase domain[19,44]. Several structures have been determined for kinase domains, both with and without bound nucleotide[26,27,32,45], but there is no structure yet of a ternary complex with both the CP and nucleotide bound. Our structure of PneKC shows that its kinase domain, similar to previously reported structures, consists of two subdomains, an N lobe that connects to the

https://doi.org/10.1038/s41467-024-51600-6

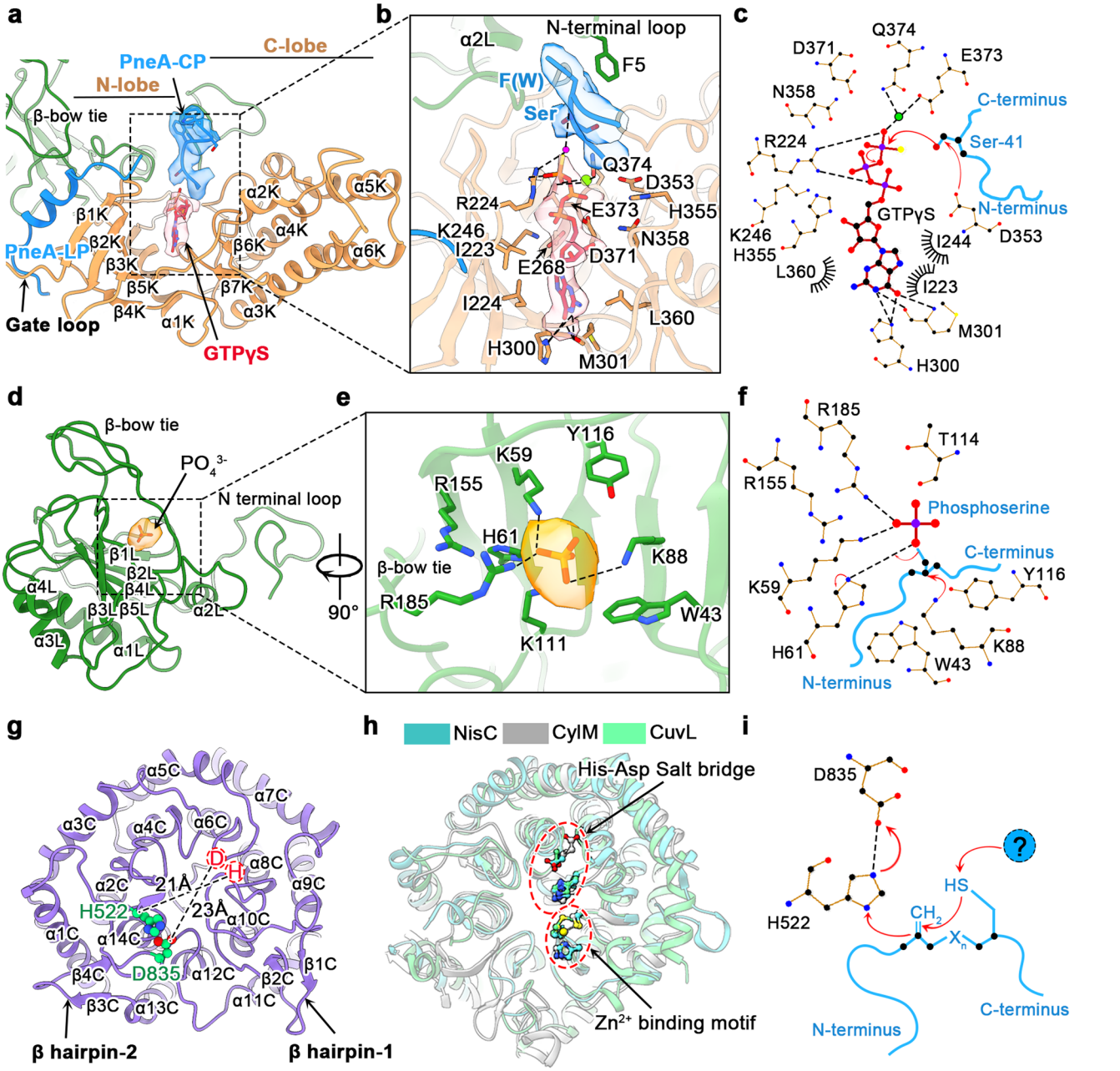

Fig. 3 | Domain structure of PneKC highlighting the noncanonical cyclase domain. a Structure of the PneKC kinase domain, comprised of an N-lobe and a C-lobe, which features a minor cleft that houses the GTP-binding pocket. **b** Detailed view of the GTP-binding site within the kinase domain, showcasing both the binding of the nucleotide and of part of the core peptide (CP). In both panels **a** and **b** the EM density for the CP region of the bound peptide and the GTPγS is shown as a blue and red surface, respectively, with 70% transparency. **c** Proposed reaction mechanism for serine phosphorylation catalyzed by the kinase domain. **d** Structure of the lyase domain with a bound phosphate. **e** Detailed view of the phosphate-binding site within the lyase domain. In both panels **d** and **e** the EM density of the bound phosphate is displayed as a yellow surface with 70% transparency. **f** Proposed reaction mechanism for the dehydration of phosphoserine, catalyzed by the lyase domain. **g** Structure of the cyclase domain of PneKC, featuring a putative catalytic His-Asp salt bridge located at a site distinct from the catalytic residues seen in conventional cyclase domains. **h** Superposition of the structures of the Zn^{2+}-dependent cyclase domains from NisC (cyan), CylM (gray), and CuvL (light green), highlighting the conserved location of the catalytic His-Asp salt bridge and the Zn^{2+}-binding motif. **i** Proposed reaction mechanism involving the noncanonical cyclase domain for Class III-b LanKCs.

lyase domain and a C lobe that connects to the cyclase domain (Fig. 3a). The overall structure of the kinase domain in PneKC resembles those of the previously identified kinase domains in Class III-a ThurKC[27] (RMSD of 3.73 Å) and Class IV CuvL[32] (RMSD of 3.75 Å). The main structural differences are observed at the GTP-binding site and the location of the gate loop (Supplementary Figs. 7b–e). Initially described for CuvL, the gate loop is the linker region between the lyase and kinase domains[26], which is disordered in the kinase domains of ThurKC[27] (Supplementary Fig. 7b) and CurKC[32] (Supplementary Fig. 7d). However, compared to the gate loop in CuvL, the gate loop in PneKC is approximately 28 residues shorter and occupies a different location. In PneKC, the gate loop sits adjacent to the interface between the lyase and kinase domains, positioned closely over the binding groove for the LP. In contrast, in CuvL, the gate loop is located far from the interface of the lyase and kinase domains, instead linking the distal side of the lyase domain to the cyclase domain (Supplementary Figs. 7a and 7e).

The C lobe features five α-helices and a β hairpin pointing toward the N lobe, forming a binding cleft for the substrate analog GTPγS. The guanine ring binds mainly to the backbone of residue Met301 (Fig. 3b). Nearby, non-polar residues, including Ile223, Ile224 and Leu360, further stabilize GTP binding. Additionally, His300 interacts directly with the O6 in GTP that is not present in ATP. Notably, a His residue at this position is specific to GTP-utilizing kinases and is not present in ATP-utilizing kinases, such as ThurKC, which has Phe311 in this position (Supplementary Fig. 7c). This His residue is the likely reason for the preference of PneKC for GTP over ATP. The residues near the triphosphate group of GTP are mostly conserved (Supplementary Fig. 7f). For example, residues Lys246 and His355 interact with the α and β phosphates, whereas Arg224, part of the P-loop, is essential for coordinating the γ phosphate. A notable interaction involves the conserved residues Glu268 from α1K, commonly referred to as helix C, and Lys246. These two residues establish an electrostatic network with the DWE motif (residues 371–373). The DWE motif is distinctive to LanKC, where it substitutes for the DFG motif that is more commonly seen in kinases[44]. A density near this motif likely represents a magnesium ion (Fig. 3b). Together, the conserved P-loop, helix C, DWE motif, and the catalytic loop (Asp353-Asn358) frame the wall of the GTP-binding cleft and ensure that its γ phosphate is optimally placed at the entrance of the cleft.

Interestingly, an additional density extends approximately 20 Å from the entrance of the cleft, adjacent to the γ phosphate of the bound GTP (Fig. 3b). The presence of two bulky sidechain densities allowed us to place the PneA CP region, spanning residues Trp37 to Trp42, into this density with acceptable fitting (Supplementary Fig. 5). In this placement, PneA residue Phe40 engages in a π-π interaction with Phe5 on the N-terminal loop of PneKC. Furthermore, Arg224 from the kinase domain, forms hydrogen bonds with the backbone of PneA residue Ser41, potentially coordinated through a water molecule. Collectively, these interactions bring PneA residue Ser41 into close proximity to the γ phosphate of GTP, priming it for phosphorylation. Upon reviewing PneA sequences, a consistent pattern emerged: an aromatic residue, either Trp or Phe, consistently precedes the Ser/Thr site designated for phosphorylation (Supplementary Fig. 1a). We thus hypothesize that this conserved motif plays a pivotal role in substrate recognition by the kinase domain of PneKC.

We used mutagenesis to validate the catalytic roles of the residues we identified. We first mutated PneKC residue Arg224 to alanine. MS analysis confirmed the complete absence of PneA phosphorylation. As control, mutations of catalytic residues in the lyase domain did not result in the loss of phosphate groups in the corresponding fragmented CP region. However, for R224A mutant of PneKC, which lacks kinase activity, no phosphorylation was detected (Supplementary Figs. 8a, b). Supporting this result, the R224A mutant exhibited significant impairment in GTPase activity (Supplementary Fig. 8c). Additionally, to confirm the catalytic role of the DWE motif in PneKC, we mutated both charged residues in the motif, Asp371 and Glu373, to alanine. This double mutant also showed significantly impaired GTPase activity. We then attempted to truncate N-terminal residues from PneKC, including Phe5, but we were not able to purify these mutants, indicating that these residues are important for the folding of PneKC.

Collectively, our results suggest a conserved phosphorylation mechanism, consistent with hypotheses proposed for other lanthipeptide modification enzymes[26,32] (Fig. 3c). The coordinated Mg^{2+} ion, partially mediated by the conserved DWE motif, activates the bound GTP by reducing the activation energy barrier for phosphoryl transfer. Based on a previous study[26], the conserved Asp353 residue (Asp349 in CuvL) from the catalytic loop then acts as a catalytic base, extracting a proton from the serine in PneA. This initiates a nucleophilic attack on the γ phosphate of GTP, ultimately resulting in the formation of a phosphoserine. Interestingly, Asp353 is positioned approximately 9.5 Å away from the target serine in the PneA peptide, indicating that it is too distant for direct nucleophilic attack. To confirm the catalytic role of Asp353, we mutated it to alanine, which impaired GTPase activity to a similar extent as the mutation of other catalytic residues, such as Asp371 and Glu373 (Supplementary Fig. 8c), thus confirming its conserved catalytic role. In PneA, either a further conformational change or the involvement of a water molecule would be necessary to mediate the nucleophilic attack.

Structure of the lyase domain reveals a bound product phosphate

Following phosphorylation by the kinase domain, the lyase domain catalyzes the β-elimination of phospho-Ser/Thr, leading to the formation of Dha/Dhb residues[32,44]. In PneKC, the lyase domain features a prominent N-terminal loop that precedes a β-sheet comprised of six antiparallel β-strands. The β-sheet is flanked by the loop region and a four α-helix bundle. The long N-terminal loop (residues 1–42) projects outward, interacting with the remote cyclase domain (Fig. 2h). It forms part of the base of the central groove shared by the three domains, likely reinforcing the stability of the multifunctional enzyme. Indeed, when we truncated the N-terminal loop, the protein aggregated and we could no longer purify it. Two other loops, the short α2L and the elongated β-bow tie, manifest a winding structure in close proximity to the kinase domain. The lyase domain ends with the α4-helix that transitions into a connecting gate loop towards the kinase domain (Fig. 3d). Structurally, the lyase domain in PneKC is similar to that in ThurKC, but distinct from that in Class IV CuvL, exhibiting an RMSD of 9.3 Å over 180 corresponding residues (Supplementary Figs. 9a, b). CuvL possesses a distinctive β-bow tie motif that projects from the lyase domain to the cyclase domain so that the three domains together form a closed ring structure[26]. In contrast, the partially unwound β-bow tie in PneKC does not contact the cyclase domain, resulting in an open protomer and the lyase and cyclase domains being far apart from each other.

Consistent with prior research[46,47], the catalytic pocket of the lyase domain is lined with many positively charged residues (Supplementary Fig. 9c) and its entrance faces the GTP-binding site of the kinase domain. This pocket is formed by eight conserved positively charged residues, namely arginine residues 99, 155, and 185, lysine residues 59, 88, 111, and 182, and His61. This positively charged pocket potentially aids the transfer of negatively charged phosphorylated substrates from the kinase to the lyase domain.

The cryo-EM map showed strong density for a phosphate molecule inside the positively charged pocket, which makes interactions with residues Lys59, His61, Lys88, and Arg185 (Fig. 3e). Sequence comparison with Class III enzymes CurKC, AciKC, and ThurKC, and Class IV enzyme CuvL also pointed to nearby residues Lys111, Tyr116, and Asp144, which are known for their role in phospho-elimination (Supplementary Fig. 9d). Additionally, conserved residues Trp43 and Tyr116 in PneKC closely interact with Lys88 and position it toward the phosphate molecule. Our map thus shows how conserved catalytic residues in the lyase domain encircle a phosphate molecule, which is a product of the β-elimination reaction. Our structure supports the β-elimination mechanism proposed in previous studies[26,44,47] (Fig. 3f), which states that two central catalytic residues are involved in converting phosphoserine to Dha. Initially, Lys88 deprotonates the α carbon of the phosphoserine, facilitating the release of the phosphate group and the formation of Dha. Then, His61, acting as a catalytic acid, donates a proton to the departing phosphate, completing the elimination process. Consistent with this mechanism, PneKC mutants H61F and K88A displayed impaired lyase activity. MS analysis revealed that while these mutants phosphorylated serine residues in PneA, they could not perform the β-elimination reaction (Supplementary Fig. 8a, b). Interestingly, unlike the K88A mutation, the H61F mutation did not significantly impact GTP hydrolysis (Supplementary Fig. 8c). To confirm this finding, we also generated a H61A mutation, which

showed a slight increase in GTPase activity, suggesting that the catalytic residues His61 and Lys88 play key roles in lyase activity but may have different roles in peptide binding, thus exhibiting different effects on GTPase activity.

Structure of the noncanonical Class III-b cyclase domain

The final modification step involves the formation of a thioether ring[24]. This is achieved through 1,4-Michael-type additions, in which Cys thiol groups react with available Dha or Dhb moieties. Typically, a consistent Cys-Cys-His zinc-binding motif coordinates a Zn^{2+} ion. This motif was first identified in Class I enzyme NisC[23] and was then also found in Class II enzyme CylM[24] and Class IV enzyme CuvL[26]. This coordinated Zn^{2+} ion acts as a Lewis acid, activating the thiol nucleophile of a Cys residue in the core peptide, which leads to a nucleophilic attack on the Dha or Dhb residue, producing an enolate intermediate. Subsequently, a conserved His residue, forming a hydrogen bond with a conserved Asp residue, catalyzes the protonation of the enolate intermediate, resulting in the formation of a cyclic thioether in the core peptide. However, LanKC enzymes lack the conventional catalytic residues and do not depend on a Zn^{2+} ion for catalysis[30,44], and the catalytic residues identified in the recent ThurKC study[27] do not seem to be present in Class III-b LanKC enzymes (Fig. 1b), leaving the catalytic mechanism enigmatic.

The cyclase domain of PneKC adopts a barrel shape, reminiscent of the previously reported structures of cyclase domains[20], and is structured around seven helix-turn-helix motifs (Fig. 3g). The loops connecting these motifs converge towards the central cavity. In Class I enzyme NisC, Class II enzyme CylM, and Class IV enzyme CuvL, these loops encircle the catalytic site (Fig. 3h). However, in line with the distinct sequences of Class III enzymes, the connecting loops in the PneKC cyclase domain do not adopt the corresponding locations (Fig. 3g). In addition, the PneKC cyclase domain features two distinct pairs of β hairpins (formed by residues Tyr725-Tyr735 and Leu823-Ile832), which are absent in other classes. Furthermore, unlike other classes, in which the catalytic residues are typically located in the large central cavity (Supplementary Fig. 10a), the central cavity in the Class III-b cyclase domain is occupied by the long α7C loop. This loop is a notable feature and appears to be exclusive to as well as conserved in Class III-b cyclase domains (Supplementary Fig. 2b). The distinct structural features of the Class III-b cyclase domain results in an RMSD value exceeding 6 Å when compared to cyclase domains of other classes.

To unravel the cyclization mechanism, we closely examined the structure of cyclase domains from other classes to identify potential catalytic residues, as these residues might also be present in PneKC albeit possibly in different positions. Our examination revealed a pair of critical residues, His522 and Asp835, that form a salt bridge. These residues are located at the base of the barrel gate, immediately adjacent to the kinase domain, but notably displaced by 21 Å (His522) and 23 Å (Asp835) from the position of the corresponding residues in cyclase domains of Classes I, II, and IV enzymes (Fig. 3g). We used mutagenesis to establish their catalytic importance. The H522A and D835A mutations not only affected the GTPase activity of the mutants but MS analysis showed that they also completely abolished their ability to catalyze cyclization (Supplementary Figs. 8a–c). Importantly, the two identified residues are key components of two signature motifs we identified for Class III-b LanKCs. His522 is part of the FPVHYYG motif at the cyclase domain's N-terminus, and Asp835 is part of the GxxxAGDxG motif near its C-terminus. We propose that these residues perform a conserved function, potentially the same function performed by the salt bridges observed in cyclase domains in other classes, by catalyzing the protonation of the enolate intermediate (Fig. 3i). However, the absence of the usual catalytic residues associated with the Zn^{2+}-binding motif and the constrained space within the conventional catalytic site suggest that the Class III-b cyclase domain utilizes a distinct mechanism. Of particular note, the residues forming the salt bridge are conserved across all Class III-b LanKCs but not in Class III-a enzymes, implying that Class III-b LanKC enzymes have a conserved but distinct cyclization mechanism (Supplementary Fig. 10b).

The leader peptide binds underneath the gate loop and adopts a helical conformation

The LP has a pivotal role in substrate recognition[16]. Previous studies, such as NMR spectroscopic studies on Class III lanthipeptide MicA in solution[34], indicated that the LP forms an amphipathic α-helix, facilitating its recognition by modification enzymes. The crystal structures of Class IV CuvA bound to CuvL[26] and Class III-a ThurA bound to the ThurKC complex[33] highlighted the significance of the highly conserved θxxθxxθ motif in LPs. It is composed mainly of hydrophobic, branched amino acids and has been shown in Class III and Class IV systems to form a helix that is critical for LP recognition by modification enzymes. Consistent with these findings, our structure also shows the LP in a helical conformation. However, since this region contains no amino acids with bulky or elongated side chains, precise modeling of this region was challenging. Nonetheless, the above-mentioned structures already showed that the conserved θxxθxxθ motif in LPs of Class III and IV lanthipeptides adopts a helical conformation and binds to a hydrophobic groove between the kinase and lyase domains of their modification enzymes[26,33]. By placing PneA residues Val5-Val11 (VxxLxxV) into the helical density, we were able to build a model for the LP region between residues 1–15 (Fig. 4). However, beyond residue 15, including LP residues 16–24 and CP residues 25–36, the density was too poorly resolved to trace the peptide backbone. Nonetheless, the density map revealed a distinct continuous density that can accommodate only several residues, featuring two bulky side chains, near the phosphorylation site in the kinase domain. We attributed this region to one of the SxxSxxxC motifs that becomes phosphorylated (Fig. 4a). Our model is consistent with the AlphaFold-Multimer[43] prediction (Supplementary Fig. 11), which also modeled the N-terminal region between residues 3–11 as an α-helix, further underscoring the utility of AlphaFold-Multimer in studying the structure of lanthipeptide systems.

The helical LP segment is located within a groove formed between the lyase domain and the β-sheet from the N-lobe of the kinase domain, known as the "primary groove" (Fig. 4a). While the density for the helical LP region is prominent in one protomer, its density is weak in the other protomer. It makes interactions with loops originating from both the lyase and kinase domains (Fig. 4b). Loops β1K and β4K from the kinase domain make direct contact with the peptide on one side, whereas loops α2L and β6L from the lyase domain make a series of interactions with the peptide on the other side, collectively securing the LP alongside the primary groove. Of particular significance is the gate loop, formed by kinase domain residues Leu205 to Phe217, which functions as a security clasp that firmly anchors the LP beneath it (Fig. 4b). Thus, by anchoring the very N-terminus through the gate loop and binding the following helical θxxθxxθ motif to the hydrophobic groove region of the kinase domain, the core peptide is directed towards the central cavity of the PneKC monomer where it can then be modified.

The helical region (residues 3–11) of the LP is predominantly hydrophobic, with only two charged residues at the N-terminus (PneA residues Glu3 and Glu4). The region of PneKC that interacts with this LP segment is also predominantly hydrophobic (Fig. 4c). The binding of the resolved LP region of PneA (residues 1–15) to the primary groove in PneKC occurs predominantly through van der Waals interactions between the hydrophobic residues of PneA and the non-polar and aromatic residues on PneKC. PneA LP residues Ala2, Val5, and Leu6 are stabilized by aromatic residue Trp219 from the β4K loop of the kinase domain; LP residue Leu6 is stabilized by aromatic residue Tyr140 from

https://doi.org/10.1038/s41467-024-51600-6

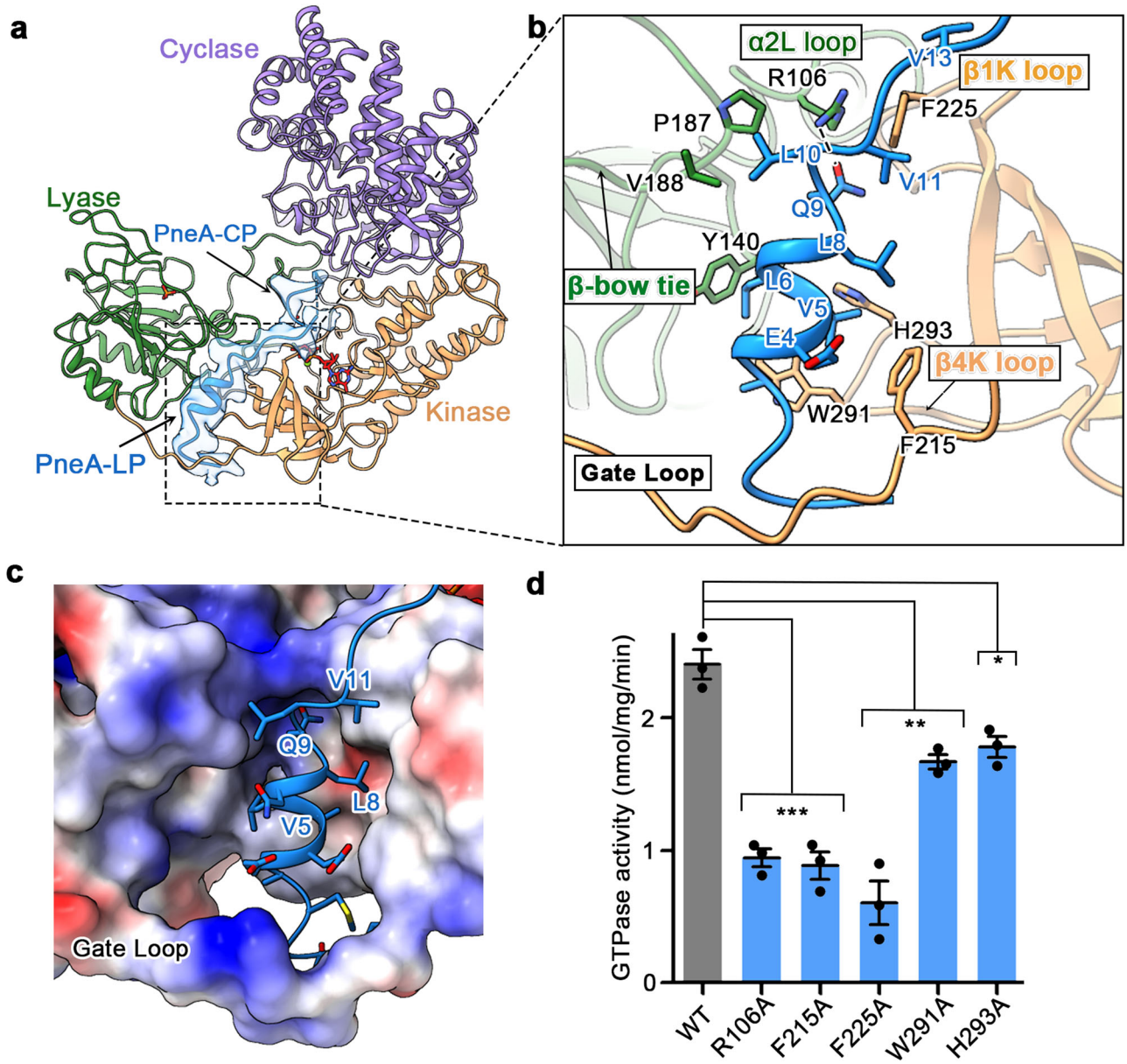

Fig. 4 | Recognition of PneA by PneKC. a PneKC protomer with bound substrate peptide, with the fully bound PneA LP assuming a helical conformation. **b** Binding of PneA to the major groove formed at the interface between the lyase and kinase domains showing that PneA makes interactions with residues coming from both the kinase and lyase domains and that the N-terminus of the LP is sealed underneath by the gate loop of the kinase domain. **c** Electrostatic potential surface shows that PneA binding is mediated by hydrophobic and electrostatic interactions **d** Effects of mutations of PneA-binding residues on the GTPase activity of PneKC. Error bars represent the standard deviation (SD) ($n = 3$), and the statistical significance was assessed using a two-tailed t-test (R106A: $p = 0.0006$; F215A: $p = 0.0009$; F225A: $p = 0.0014$; W291A: $p = 0.0062$; H293A: $p = 0.0157$). Source data are provided as a Source Data file.

the α3L loop of the lyase domain; LP residue Leu10 is stabilized by the hydrophobic environment provided by residues Val188 and Pro187 from the β bow-tie of the lyase domain; and LP residues Val11 and Val13 form hydrophobic interactions with Phe225 from the β1K loop of the kinase domain. Additionally, LP residue Glu4 makes a π-anion interaction with Phe215 on the gate loop, and LP residue Gln9 hydrogen bonds to Arg106 on the α2L loop of the lyase domain. Furthermore, Phe225 forms a π-cation interaction with Arg106, likely contributing to the unwinding of the α-helix of PneA, similar to the function of Phe236 reported for ThurKC[33], thereby allowing the PneA CP to become accessible to the catalytic domains in PneKC. Mutation to alanine of residues Arg106, Phe215 and Phe225, which are all involved in making strong interactions with the bound PneA peptide, significantly impacted the GTPase activity of PneKC, reducing it to approximately one-third of that observed for wild-type PneKC, confirming their key role in LP binding (Fig. 4d). On the other hand, PneKC mutants in which residue Trp291 or His293, both involved in hydrophobic interactions with PneA, were mutated to alanine exhibited only a modest decrease in GTPase activity (Fig. 4d).

Interestingly, LP binding in PneKC closely resembles that seen in the recent structure of Class III-a ThurKC[33] but differs from that seen in Class IV CuvL[26]. In CuvL, the very N-terminal region of the LP (residues 1–8) encircles the N-lobe of the kinase domain at the bottom of the enzyme, a region that does not exist in PneA (Supplementary Fig. 7b and 7e). Instead, in PneKC, the very N-terminal region of the LP interacts with the gate loop, which locks the LP underneath it (Supplementary Fig. 7e). Despite this difference, PneKC, similar to Class III-a ThurKC[33] and Class IV CuvL[26], and possibly also similar to Class II

https://doi.org/10.1038/s41467-024-51600-6

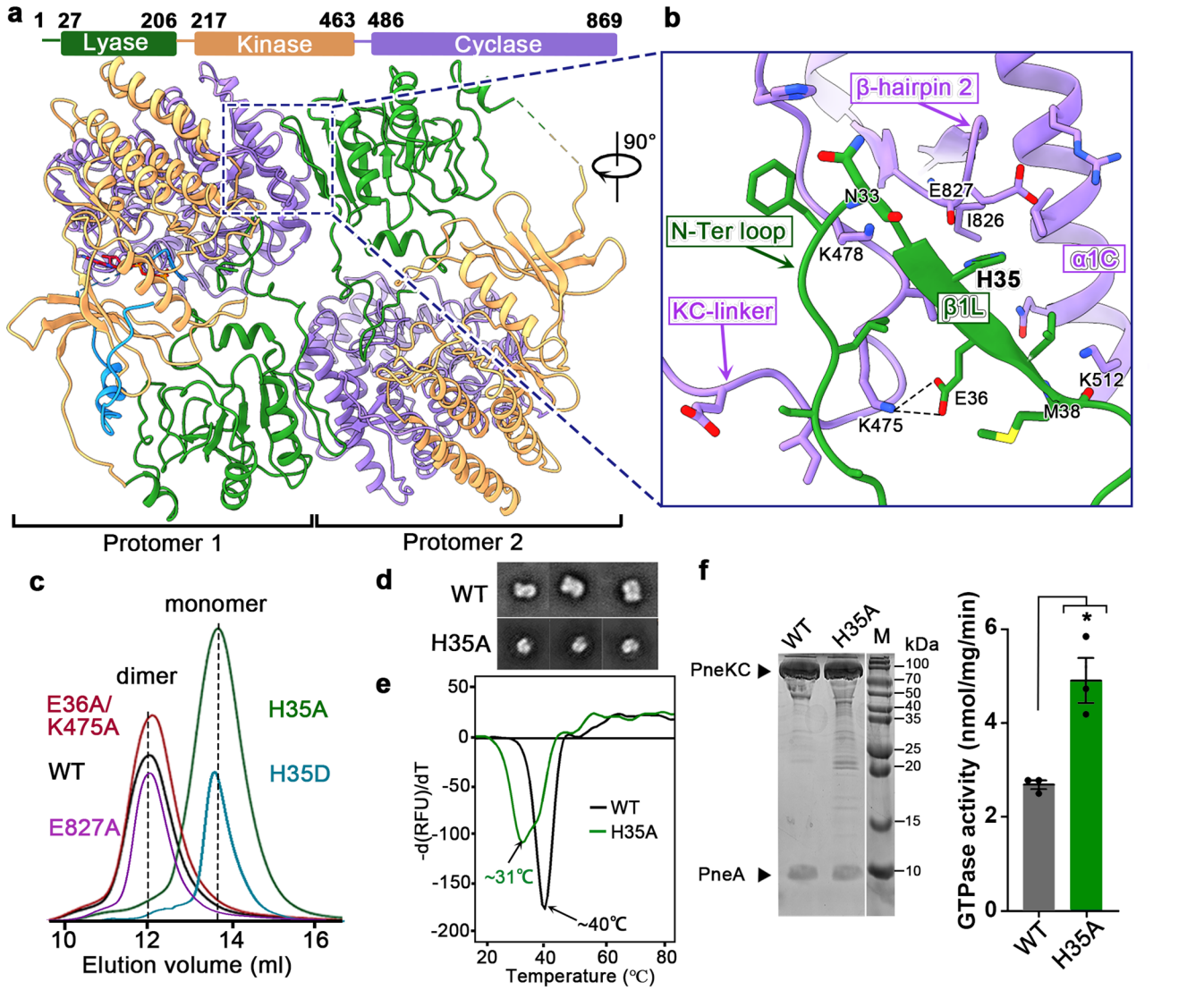

Fig. 5 | Identifying His35 as a hot spot for PneKC dimerization. a The PneKC dimer is stabilized by two symmetric interaction interfaces between the lyase and cyclase domains. **b** The PneKC dimerization interface is formed by the N-terminal loop of the lyase domain and the KC linker and β-hairpin 2 of the cyclase domain. Residue His35 from the lyase domain of one protomer interacts with three motifs from the cyclase domain of the other protomer. **c** Size-exclusion chromatography profile of PneKC with mutations of interface residues, showing that mutation of His35 to alanine and aspartate disrupt dimerization. **d** 2D-classs averages of wild-type PneKC forming a dimer and H35A mutant PneKC forming a monomer. **e** DSF melting curves for the thermal unfolding of wild-type and H35A mutant PneKC, showing that dimeric wild-type PneKC has higher thermostability. **f** GTPase activity of dimeric wild-type and monomeric H35A mutant PneKC in the presence of equal amounts of PneA, with a PneKC monomer to PneA ratio of 1:1. The monomeric H35A mutant PneKC exhibits approximately twice the level of GTPase activity as the dimeric wild-type protein. Error bars represent the standard deviation (SD) ($n = 3$), and the statistical significance was assessed using a two-tailed t-test ($p = 0.02$), suggesting negative cooperativity for GTP hydrolysis in the dimer. To ensure that the same amount of protein and peptide were used in these assays, the protein concentrations were assessed by quantitative SDS-PAGE. Source data are provided as a Source Data file.

HalM2[25], recognizes the LP predominantly through hydrophobic interactions, which is facilitated by the LP forming a helix. This mechanism differs from that of most other Ribosomally Synthesized and Post-translationally Modified Peptide (RiPP) enzymes[16], including the Class I enzyme NisB[21], which employs a RiPP precursor peptide recognition element (RRE) for recognition of the substrate peptide.

In summary, similar to Class III-a ThurKC[33] and Class IV CuvL[26], both the lyase and kinase domains in PneKC contribute to the recognition of PneA. In particular, the N-terminus of the bound LP is locked in its position by the gate loop. In this state, the LP region of the bound PneA (Residues 3–11) adopts a helical conformation. This structure is stabilized mainly by hydrophobic interactions. Upon binding, the very N-terminal region (Residues 1–11) of the LP sits in a groove between the lyase and kinase domains and positions the C-terminal CP close to the three catalytic pockets, preparing it for subsequent modifications.

The PneKC dimer uses a negative cooperativity mechanism

To investigate the dimerization mechanism of PneKC and its potential biological significance, we examined the dimer interface. Our analysis revealed that dimerization is mainly mediated by the lyase domain of one protomer interacting with the cyclase domain of the other (Fig. 5a). Interface analysis using PISA[48] indicated a substantial interface area between the two protomers of 1139.4 Å^2. The dimer is primarily formed by the N-terminal loop and the adjacent β1L of the lyase domain from one protomer interacting with three motifs from the cyclase domain of the opposite protomer, namely β-hairpin 2, the kinase-cyclase (KC) linker, and the α1C helix (Fig. 5b). These interactions are primarily hydrophobic in nature, with only one salt bridge between Glu36 and Lys475 and several hydrogen bonds, including Lys478 with Asn33 and Lys512 with Met38. In addition, His35 forms a hydrogen bond with the backbone carbonyl group of Ile826, and its

side chain interacts with Glu827. Positioned at the center of the dimer interface, His35 extends its side chain to within 5 Å of all three interacting motifs from the other protomer, the α1C helix, β2 hairpin, and KC linker. This position suggests an essential role for His35 in the stabilization of the dimer. Our mutagenesis experiments indeed support the significance of His35 for dimerization. Mutations such as H35D and H35A significantly impaired dimer formation, while mutations of residues interacting with His35, i.e., E36A/K475A and E827A showed minimal to no effect on dimerization, as assessed from shifts in the SEC profiles and negative-stain EM imaging (Figs. 5c, d). These results suggest that the salt bridge between Glu36 and Lys475 and the interaction between His35 and Glu827 are not critical for dimerization. Instead, it is the extensive van der Waals interactions and hydrogen bonds between His35 and residues from all three motifs from the opposing protomer that contribute most to dimerization, identifying residue His35 as the most critical "hot spot" for PneKC dimerization.

To understand the biological significance of the dimer formed by PneKC, we first used differential scanning fluorimetry (DSF) to assess the thermostability of both the dimeric wild-type protein and the monomeric H35A mutant (Fig. 5e). The wild-type dimer exhibited a thermal-unfolding temperature of ~40 °C, while the H35A mutant displayed a thermal-unfolding temperature of ~31 °C, demonstrating reduced stability under heat stress. We then measured the GTPase activity in the presence of PneA for both the dimeric wild-type protein and the monomeric H35A mutant, with the molar PneKC monomer to peptide ratio set at 1:1 (Fig. 5f, left). Surprisingly, the monomeric H35A mutant was not only active but displayed twice the GTPase activity of dimeric wild-type PneKC (Fig. 5f, right). Together with our co-expression of PneKC with PneA, where SDS-PAGE and cryo-EM analysis revealed that only one PneA binds to a PneKC dimer (Supplementary Figs. 3b and 4b), these results imply that only one of the protomers in the PneKC dimer is active at any given time. As our structure also showed that the PneA substrate peptide predominantly binds to only one protomer, we propose that the PneKC dimer operates via a negative cooperativity mechanism, in which the two protomers alternate in their function, so that only one is active at any given time.

Mechanistic details of the negative cooperativity mechanism

To investigate the putative negative cooperativity mechanisms of PneKC for peptide modification, we added a three-fold molar excess of PneA to PneKC in the presence of 1 mM GTP/Mg^{2+} to sustain a continuous modification reaction. We prepared samples from this mixture that we analyzed by cryo-EM. The resulting density maps revealed two main conformations (Figs. 6a–c and Supplementary Fig. 12), representing two distinct structural states of the enzyme, each offering distinct insights.

The first state, resolved at a resolution of 3.8 Å, had no peptide bound but revealed weak nucleotide density in one of the protomers. We designated this state as the "pre-binding state" (Fig. 6b). The second state, resolved at a resolution of 4.0 Å, showed density for the LP and nucleotide in one protomer, while the other protomer showed density for neither. Neither protomer showed any density for the CP. We therefore refer to this state as the "LP-bound" state (Fig. 6c). The observation that only one protomer in the LP-bound state displayed LP binding, provides further support for our proposed negative cooperativity modification mechanism (Supplementary Fig. 13a). Interestingly, while in both the pre-binding and LP-bound states, ligands were observed mainly in one protomer, both protomers in the dimer adopted nearly identical conformations (Fig. 6d).

Comparison of the pre-binding and LP-bound states revealed a notably different dimer configuration (Fig. 6e). Specifically, the cyclase domains in the LP-bound state moved closer to each other by approximately 10.6 Å, as measured for residue Leu645 on the α7C helix of the cyclase domain (Fig. 6e). Further comparison of the two states also revealed a 6.5-Å shift of the lyase domain towards the cyclase domain, as measured for residue Gln127 (Fig. 6f). Peptide binding thus appears to induce a conformational shift in the protein, resulting in a "tense" state that is characterized by a shorter distance between the cyclase and lyase domains. Importantly, as both protomers within each state assume the same conformation, the tense configuration adopted by one protomer upon ligand binding appears to be allosterically transmitted to the neighboring protomer, resulting in a constricted primary groove that might be less favorable for peptide binding (Fig. 6g). Structure of enzymes in the presence and absence of bound peptide have previously been obtained for Class III-a enzyme ThurKC[33] and Class IV enzyme CuvL[26], but the structures showed different effects of peptide binding. In Class IV CuvL, peptide binding did not induce a meaningful change in overall conformation. While changes in overall conformation were detected in ThurKC upon peptide binding, these differ from the ones we observe in PneKC. Specifically, ThurA binding induced ThurKC to adopt a more relaxed conformation compared to the peptide-free state, with the N-lobe of the kinase domain together with the lyase domain moving away from the C-lobe of the kinase. Thus, peptide binding can have very different effects on modification enzymes, potentially indicating variations also in the allosteric effects on enzyme function.

To elucidate the potential mechanism underlying the transition from the relaxed to the tense state, we analyzed the two structures in more detail. We noticed no obvious conformational changes at the dimer interface upon peptide binding (Fig. 6e), suggesting that the transition from the relaxed to the tense state primarily occurs in the peptide-bound protomer. We then carefully inspected the components that link the lyase domain to other domains, and found that neither the N-terminal region nor the gate loop of PneKC exhibited significant conformational changes upon peptide binding (Supplementary Fig. 13b, left). Instead, we found that peptide binding induces the formerly disordered β-bow tie to adopt an almost fully ordered conformation, establishing direct interactions with the substrate peptide from the side of the lyase domain (Supplementary Fig. 13b, right). Moreover, on the opposite side, the substrate peptide is anchored to the N lobe of the kinase domain, where no obvious overall conformational changes occur despite local changes at the GTP-binding site (Supplementary Fig. 13c). We therefore hypothesize that the interaction between the β-bow tie and the bound peptide serves as the driving force for the conformational switch between the relaxed and tense states namely by pulling the lyase domain towards the peptide-bound kinase/cyclase domain. As the peptide-bound protomer transitions into the tense state, this conformational alteration is transmitted to the other protomer through the dimeric interface, resulting in a tense conformation that is characterized by a more compact interface between the kinase and lyase domains (Fig. 6e). This conformational change may hinder peptide binding to the opposing protomer while promoting the ordering of the catalytic domain within the PneA-bound protomer (see below). This phenomenon likely contributes to the negative cooperativity between the two protomers within the dimer.

Structural dynamics of PneA recognition and its GTPase activity modulation

So far, we have characterized three distinct states of PneKC in relation to PneA binding: the pre-binding state, the LP-bound state, and a state trapped with GTPγS in which both the LP and CP segments are captured (Fig. 7a). For clarity, we refer to this latter state as the "fully-recognized" state as the CP in this state is already positioned for modification. Notably, in both the LP-bound and fully-recognized states, the peptide predominantly binds to just one protomer, consistent with the negative cooperativity mechanism. These states enable us to explore the dynamics of both PneKC and PneA during the substrate-recognition process.

https://doi.org/10.1038/s41467-024-51600-6

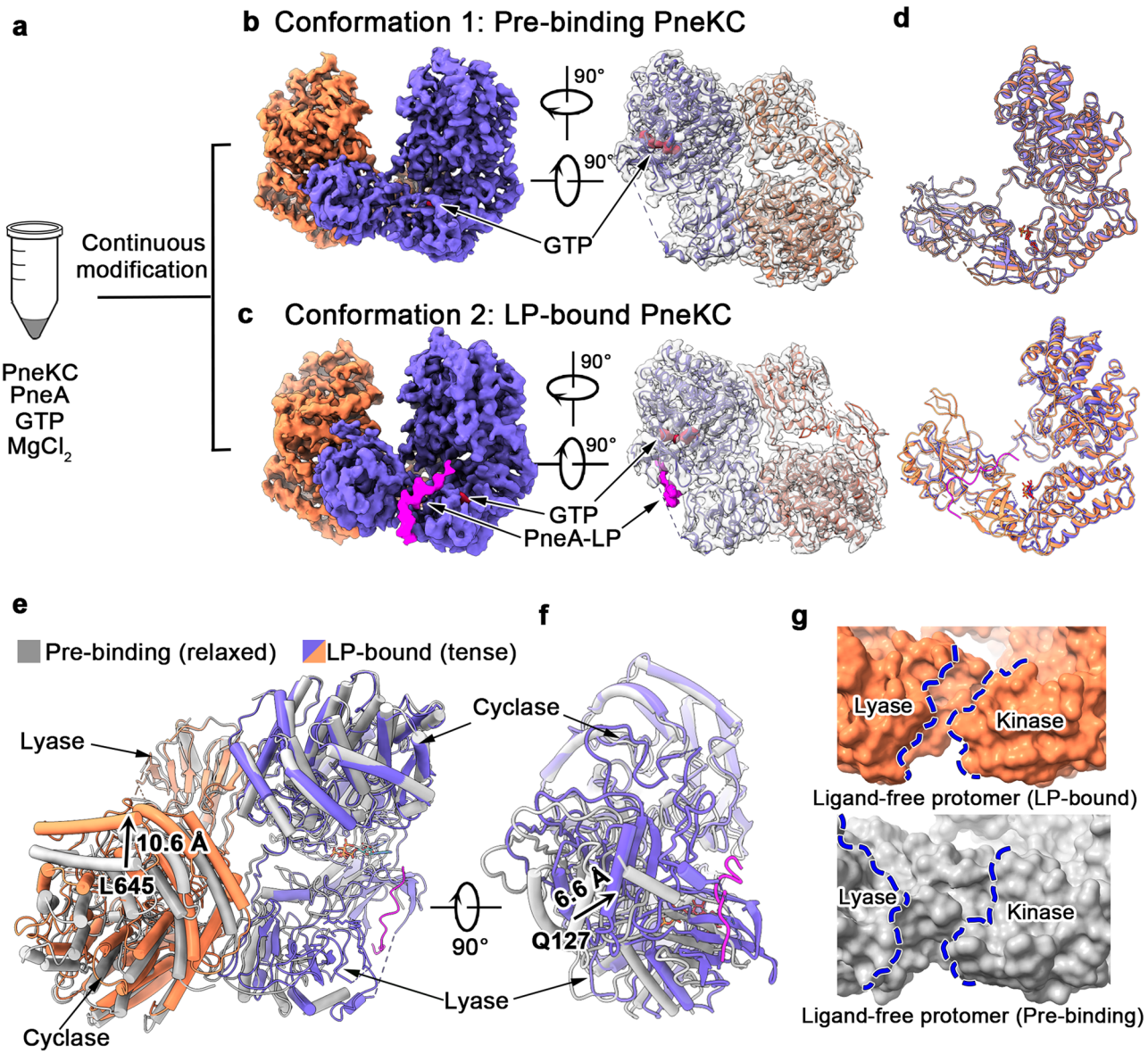

Fig. 6 | Inter-protomer allosteric regulation in response to peptide binding. **a** PneKC sample catalyzing sustained PneA modification that was used for cryo-EM imaging that led to the identification of two distinct conformations that both show ligand bound only in one protomer. **b** Density map of conformation 1 with one protomer showing density for GTP (purple/red) but not the other protomer (orange). **c** Density map of conformation 2 with one protomer showing density for both GTP and PneA (purple/red/magenta) while the other protomer again shows no density for ligands (orange). **d** Superimposition of the two protomers within each conformation. Both protomers exhibit a relaxed conformation in the PneKC pre-binding state (RMSD: 1.06 Å) and a tense conformation in the LP-bound state (RMSD: 1.09 Å). **e** Superimposition of pre-binding PneKC (gray) with LP-bound PneKC (purple/coral) with focus on one side of the cyclase domain, showing an overall contraction of 10.6 Å induced by PneA binding as measured by the movement of cyclase domain residue Leu645. **f** Superimposition of the GTP-bound protomer of the pre-binding state with the ligand-bound protomer of the LP-bound state focusing on the cyclase domain. The movement of residue Gln127 reveals a contraction by 6.6 Å. **g** Surface view of the ligand-free PneKC protomer from the Pre-binding (gray) and the LP-bound (orange) states, showing an allosterically induced contraction of the primary groove.

In the pre-binding state, several regions in the lyase and kinase domains are disordered, including the long β-bow tie (Arg160-Asp199), the gate loop on the N-terminal side of the kinase domain (Leu205-Asp220), and portions of the β2K loop in the kinase domain between Lys237 and Gly240 (Fig. 7a). In this state, PneKC adopts a relaxed conformation in which the primary groove is wide open and easy for peptides to access.

Upon PneA binding and transitioning to the LP-bound state, the β-bow tie begins to order and to form direct interactions with the bound PneA, as evidenced by the stronger density for the Arg160-Val176 and Glu179-Asp199 regions in the lyase domain. Clear density was also observed for the entire kinase domain, which made it possible to model its entire sequence (Fig. 7a). For PneA, density is only observed for the N-terminal region of the LP, while there is no clear density for the C-terminal parts of PneA, including the CP, suggesting that these are highly flexible. In this state, the bound LP adopts an extended rather than a helical conformation. This may reflect the initial recognition of PneA, which may occur through non-specific interactions between hydrophobic residues in the LP and the predominantly hydrophobic pocket in the primary groove. Upon LP binding to the primary groove between the lyase and kinase domains in one protomer, both protomers will switch to the tense conformation.

In the fully-recognized state, all the loops that were disordered in the pre-binding state become ordered through direct interactions

https://doi.org/10.1038/s41467-024-51600-6

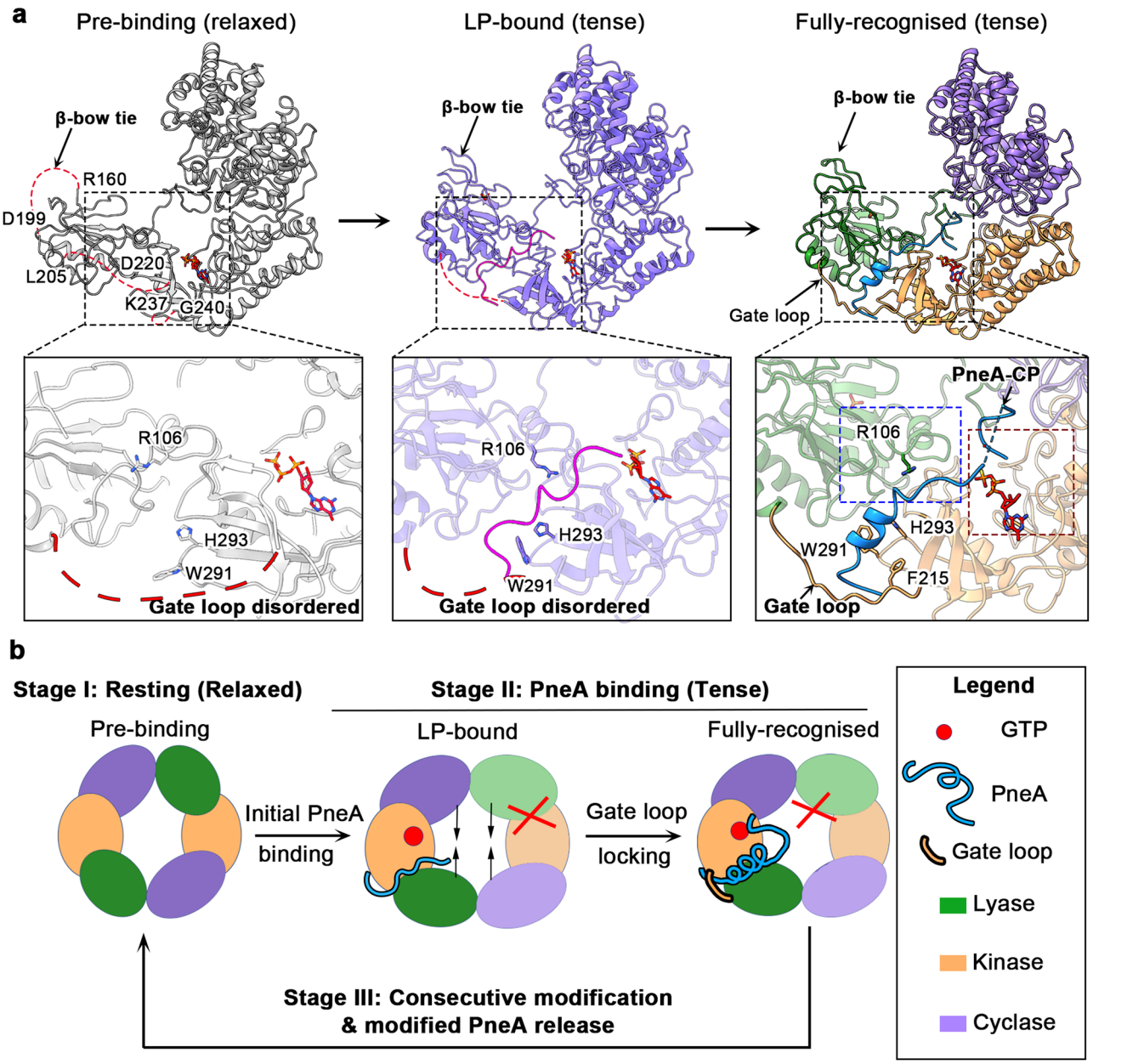

Fig. 7 | Conformational dynamics of PneKC and PneA during peptide binding: towards a working model for lanthipeptide modification by PneKC. a Steps in the binding of PneA to PneKC, which show a progression from the pre-binding state, in which loops at the primary groove are largely disordered, to the LP-bound state, in which the PneA-binding loops become ordered while PneA LP exists in an extended conformation, to the fully-recognized state, in which all the PneA-binding loops are ordered and PneA LP adopts a helical conformation that is sealed underneath the gate loop. **b** A working model for initial PneA recognition and subsequent modification by the PneKC dimer based on a negative cooperativity mechanism.

with the bound PneA (Fig. 7a). In particular, the gate loop is in position to lock the N-terminus of the bound peptide underneath, and the CP localizes to the kinase domain, ready to be modified. The interactions with the loops not only stabilize the binding of PneA but also frame the catalytic site of both the lyase and the kinase domains. Residues surrounding the binding groove, such as Trp291 and His293 from the β4K loop, shift to accommodate PneA binding (Supplementary Fig. 14a). Phe225 from the β1K loop moves downward by 2.5 Å towards PneA, while Arg106 from the α2L loop undergoes a 90-degree rotation to orient itself toward the incoming substrate (Supplementary Fig. 14b). With these extensive interactions in place, the LP region encompassing residues 3-11 adopts a helical conformation. These structural changes complete the full binding of PneA and position the CP next to GTP for further processing. Simultaneously, the GTP-binding site undergoes local conformational changes. Residue Arg224 moves by 2.4 Å closer to Asp371, which is located opposite the GTP-binding site, potentially preparing the catalytic site of the kinase domain to phosphorylate the bound peptide (Supplementary Fig. 14c). A recent biochemical study on ThurKC[33] elegantly demonstrated that binding of the LP alone induces conformational changes that facilitate catalytic activity through the organization of interdomain interactions. Despite efforts to generate PneA LP truncations similar to those reported for ThurA LP, we were not able to obtain soluble LP. While we have no direct evidence, our structure of LP-bound PneKC that only reveals density for LP, together with the strong binding of LP observed in the structures of PneKC in both the LP-bound and fully recognized states, suggests that LP binding may play a key role in inducing

the allosteric conformational changes in PneKC, similar to those observed in ThurKC.

All our structures reveal that a "match-and-fit" mechanism governs the recognition of PneA by PneKC, which is characterized by significant dynamics in the enzyme. Several crucial loops of the lyase domain and the gate loop of the kinase domain, all initially disordered, adopt well-defined conformations upon PneA binding and lock the N-terminus of the bound PneA LP underneath the gate loop. Simultaneously, local conformational changes occur at the GTP-binding site, preparing the catalytic site of the kinase domain to phosphorylate PneA, the first step in the peptide modification reaction catalyzed by PneKC.

Discussion

Our study identifies distinct types of LanKCs and offers in-depth insights into the lanthipeptide modifications carried out by the characterized dimeric Class III-b LanKC enzyme, enriching our understanding of lanthipeptide processing. Our structures allow us to describe the steps during peptide recognition by PneKC, which may be conserved across all Class III-b LanKCs (Fig. 7b). In the model we propose, PneKC undergoes distinct stages during peptide recognition and modification. Initially, in a resting state without ligand (Stage 1), PneKC adopts a relaxed conformation with the substrate-binding site being largely disordered. In stage 2, peptide and nucleotide bind to one protomer, as seen in our LP-bound structure. The LP binds to one protomer in an extended conformation, and key binding motifs, including the gate loop, are not optimally positioned. However, early interactions, such as those between the β-bow tie from the lyase domain and the bound peptide, may induce the lyase domain to move towards the central groove, resulting in the LP-bound protomer adopting a "tense" conformation, which is propagated through the dimer interface to the other protomer. This conformational change appears to block peptide access to the groove in the second protomer, causing the observed "negative cooperativity". At stage III, the bound LP adopts a helical structure between residues 3-11, enabling full binding. Simultaneously, the gate loop that connects the lyase and kinase domains becomes organized, sealing the N-terminus of the bound peptide underneath and positioning the CP region at the kinase catalytic site for modification.

Our study does not capture the following consecutive catalysis process, but our structure of PneKC with partial density for one of the phosphorylation sites of the CP provides insights into potential binding of the substrate peptide and the shuttling of intermediates between different domains. Specifically, we observe an aromatic residue that precedes the conserved SxxSxxxC motif in the CP region of PneA that is targeted for modification, which could engage in π-π interactions with Phe5 on PneKC, priming the following Ser residues for phosphorylation. A bulky aromatic amino acid before Ser/Thr residues is observed in many Class III-b enzymes (Supplementary Fig. 2c), suggesting a common mechanism for how the kinase domain detects the CP. Class III-a enzymes and enzymes from other classes lack these patterns, indicating the evolution of distinct substrate recognition mechanisms. After phosphorylation of PneA, negatively charged intermediates migrate to the lyase domain's positively charged catalytic pocket, facilitating Dha/Dhb intermediate formation. Subsequently, the Dha/Dhb intermediate, possibly due to its neutral charge following Ser/Thr modification, may no longer associate with the kinase or lyase domains. Instead, it would shuttle to the cyclase domain for the final cyclization step. Further investigations into peptide binding at different domains from various systems are needed to fully understand the specific peptide recognition and modification mechanisms for each domain.

Apart from monofunctional NisB[21], PneKC represents a notable case in which a multifunctional lanthipeptide modification enzyme forms a dimer. This contrasts with other studied lanthipeptide modification enzymes, such as ThurKC and CuvL, which primarily exist as monomers. These findings suggest a divergence in assembly not only among Class III LanKC enzymes but potentially across other classes as well. Our study shows that the dimer has higher thermal stability than the monomer (40 °C *versus* 31 °C). Considering that *Streptococcus pneumoniae*, a human pathogen, typically grows at a temperature of ~33 °C and can survive in the human body at 37 °C, the advantage of the PneKC dimer becomes apparent. The evolution of a dimer that confers higher stability to PneKC overcomes the thermal liability of the enzyme and creates a crucial advantage for the pathogen's survival.

Our study identified His35 as a hot spot residue for the dimerization of PneKC. His35 as well as many other dimer interface residues are conserved in many Class III-b LanKCs (Supplementary Fig. 15), suggesting that most Class III-b enzymes may also exist as dimers. Interestingly, His35 is replaced by aromatic or acidic residues in some Class III-b LanKCs. Further investigation is needed to confirm whether this hot spot residue can be utilized to predict the oligomeric state of Class III-b LanKCs and modification enzymes from other classes.

In our study, we identify three motifs in Class III-b LanKCs that are absent in other LanKCs and may thus be signature motifs for this particular LanKC class. In particular, residues His522 and Asp835, part of two of these motifs form a critical salt bridge that is crucial for PneKC to catalyze the cyclization reaction. This salt bridge not only sheds light on the function of the noncanonical cyclase domain in Class III-b LanKCs but also underscores the significance of the identified signature motifs for catalysis, reinforcing the distinctness of this LanKC subclass. Furthermore, the yet-to-be-identified residues responsible for the catalytic roles usually associated with the Zn^{2+}-binding motif, together with the obstruction of the cavity that usually harbors the catalytic site by the distinctive α7C loop, further support the notion that the Class III-b cyclase domain uses a distinct mechanism. The structure of a cyclase domain from a Class III LanKC in complex with a peptide substrate has the potential to resolve many of these questions. While additional research is needed to unravel the precise cyclization mechanism, our current study has already significantly enhanced our understanding of the dynamic processes underlying peptide recognition and domain coordination within lanthipeptide modification enzymes. Moreover, considering the high potential of lanthipeptides in antimicrobial applications, these insights pave the way for the development of Class III-b lanthipeptides for antimicrobial purposes.

Methods

Sequence analysis and phylogeny reconstruction

Maximum likelihood phylogeny trees were calculated using the ClustalW[49] online tool, using previously published LanKC sequences[36,50] and sequences provided by the NCBI. Multiple sequence alignment of selected sequences was performed using ClustalX[51] and visualized using ESPript 3.0[52].

Cloning and mutagenesis

The full-length sequences of PneKC (NP_358798.1) and PneA (WP_004264816.1) were amplified from *Streptococcus pneumoniae* genomic DNA obtained from ATCC (ATCC 6314), via PCR using custom-synthesized primers (Supplementary Table 1). Recombination was then performed to insert the genes of interest into pET28a(+) and pQLinkN vectors with an N-terminal histidine tag (six-His tag for pET28a(+), seven-His tag for pQLinkN). For the co-expression of PneKC and PneA, the two genes were first inserted separately into the pQLinkN vector and subsequently linked together to obtain the pQLinkN-PneKC-PneA construct (Supplementary Table 1); a pQLinkN-PneKC-PneA construct with a His7 tag only on PneKC was also generated to purify the PneKC/PneA complex without a His tag on PneA.

To generate mutants, pQLinkN-PneKC was used as a template and amplified using primer sequences listed in Supplementary Table 1. Mutant sequences produced by PCR were digested with Dpn1 for 30 min at 37° and then used for transformation. The sequence of all the constructs was verified by DNA sequencing (BioBasic).

To maintain consistency in our mass spectrometry studies, we exclusively used purified PneA expressed from the pQLinkN vector, which contained an N-terminal His_7 tag. PneA used for functional studies and for the structural analysis of the pre-binding and the LP-bound complexes, except for those co-expressed with PneKC, were purified from the pET28a-PneA construct with an N-terminal His_6-tag. For the structure of the full bound complex, the pQLinkN-PneKC-PneA construct was used with an N-terminal His_7 tag on PneA.

In all PneKC constructs, we inserted a long flexible linker sequence (GAAGTSLYKKAGENLYFQG) between the His tag and PneKC. This design ensured optimal exposure of the His tag for purification, resulting in high purity and yield of PneKC. For our functional and structural analyses, we used purified PneKC with the N-terminal His tag. However, due to the instability of purified His-tagged PneKC after cleavage of the His tag, we generated a pQLinkN-PneKC-PneA construct by mutating the start codon preceding the His tag. This allowed us to purify PneKC without a His tag, which served as control to confirm that the presence of a His tag did not interfere with PneKC function. Importantly, our analysis revealed no difference in the dimerization and GTP hydrolysis activity of purified PneKC in the presence or absence of an N-terminal His tag (Supplementary Figs. 3b, 3e, and 3f), demonstrating that we could use His-tagged protein for our studies.

Expression and purification of PneKC with or without PneA

The pET28a-PneKC or pQLinkN-PneKC-PneA (WT&mutants) constructs were used to transform *E. coli* BL21(DE3) competent cells and amplified in 1 l Luria-Bertani (LB) medium supplemented with 0.5 μg/ml kanamycin and ampicillin. The cells were grown at 37 °C until the optical density at 600 nm (OD_{600}) reached 0.8, after which the culture was cooled to 16 °C and induced by adding isopropyl β-d-1-thiogalactopyranoside (IPTG) to a final concentration of 0.5 mM. After 18 h of incubation, the cells were harvested by centrifugation and the cell pellet was resuspended using lysis buffer (40 mM Tris-HCl, pH 7.5, 200 mM NaCl, 1 mM DTT) and lysed using a high-pressure homogenizer. The cell debris was removed through centrifugation at 20,000 × *g* for 1 h and the soluble fraction was incubated with 1 ml Co-NTA affinity resin for 2 h at 4 °C with constant shaking. After incubation, the resin was washed 5 times with 10 column volumes (CV) of lysis buffer. The bound protein was then eluted using 2 CV of elution buffer (40 mM Tris, pH 7.5, 200 mM NaCl, 250 mM Imidazole) and concentrated to 1 ml using a 30-kDa cut-off concentrator. The purified protein was applied to a Superdex™ 200 Increase 10/300 GL gel filtration column connected to an ÄKTA Go Protein Purification System (Cytiva) (20 mM Tris-HCl, pH 7.5, 200 mM NaCl). The protein concentration was determined using a Nanodrop spectrophotometer at a wavelength of 280 nm, following baseline correction with blank buffer. Absorbance readings were converted to protein concentrations using the Beer-Lambert law with the corresponding extinction coefficient estimated using the Expasy online tool (https://web.expasy.org/protparam/).

Expression and purification of PneA

pET28a-PneA or pQLinkN-PneA were also expressed using *E. coli* BL21(DE3) competent cells. Cells were grown at 37 °C until an OD_{600} of 0.3 was reached and induced with 1 mM of IPTG. After 4 h of incubation at 37 °C, the cells were harvested by centrifugation. The cell pellet was resuspended using lysis buffer and lysed using a high-pressure homogenizer. The insoluble fraction was harvested by centrifugation at 20,000 × *g* and resuspended in denaturation buffer (8 M urea, PBS, pH 6.8). The resuspended pellet was sonicated for 5 min at 20%, followed by centrifugation at 20,000 × *g*. The supernatant was incubated with 1 ml Co-NTA affinity resin for 1 h at room temperature with constant shaking. After incubation, the resin was washed 5 times with 10 CV of denaturation buffer, followed by elution using 2 CV of urea elution buffer (8 M urea, PBS, 250 mM Imidazole, pH 6.8). Finally, the purified protein was dialyzed overnight against lysis buffer using 3500 molecular weight cut-off dialysis tubing. The dialyzed protein was concentrated to 0.5 mg/ml as assessed with a Nanodrop spectrophotometer at a wavelength of 280 nm.

Size-exclusion chromatography (SEC)

A Superdex™ 200 Increase 10/300 GL gel-filtration column was calibrated using a high molecular weight gel filtration calibration kit (Cytiva) with a flow rate of 0.5 ml/min. The standards used were thyroglobulin (669 kDa, elution volume: 9.3 ml), ferritin (440 kDa, elution volume: 10.5 ml), aldolase (158 kDa, elution volume: 12.4 ml), conalbumin (75 kDa, elution volume: 13.9 ml), and ovalbumin (43 kDa, elution volume: 14.9 ml). The resultant peaks were used to estimate the oligomeric state of PneKC based on the elution profile. His-tagged wild-type PneKC eluted at 12.1 ml and H35A mutant PneKC at 13.3 ml, corresponding to ~200 kDa.

Nucleotide hydrolysis assay

The Malachite green phosphate assay was performed to determine the level of inorganic phosphate produced by GTP/ATP hydrolysis[53]. All experiments were performed at room temperature, and three independent replicates were conducted for each hydrolysis assay. PneKC at 25 μM was used for the NTPase activity assay in the absence of PneA. For all subsequent assays in the presence of PneA, 2.5 μM of PneKC dimer was used per reaction, supplemented with 5 μM (for a PneKC monomer to PneA ratio of 1:1) or 15 μM (for a PneKC monomer to PneA ratio of 1:3) PneA. The 20-μL reaction mixture was supplemented with 1 mM NTP, 1 mM $MgCl_2$ and 1 mM DTT and incubated at room temperature. After 1 h of incubation, 80 μl Malachite green-ammonium molybdate (MG-AG) solution was added and vortexed immediately to inactivate the enzyme. After 2 min, 10 μl 34% (w/v) sodium citrate was added and immediately vortexed. After 5 min, the absorbance at 650 nm was measured. The amount of inorganic phosphate (Pi) released was calculated using a standard curve generated with known amounts of Pi using a K_2HPO_4 solution. Data were fitted to the Michaelis–Menten equation using Microsoft Excel and GraphPad Prism 5.

To ensure consistency in the amount of PneA used across different assays within the same experiment or with specific PneKC and PneA ratios, we implemented a three-step approach. First, the protein concentration was estimated using a Nanodrop spectrophotometer, as described above. Next, SDS-PAGE was performed to visualize the amount of PneKC and PneA applied in all reactions within the same set of experiments, with their quantities estimated by visual inspection. Finally, to precisely determine the PneKC to PneA ratio for each assay, quantitative analysis was conducted. This involved assessing the intensity of the two protein bands on SDS-PAGE gels, measured in terms of pixel density relative to their molecular weights. Following gel electrophoresis and staining, the protein bands were imaged using Image Lab software (Bio-Rad). A rectangular selection was drawn around each band of interest, and its pixel density was quantified and normalized to the molecular weight of the corresponding protein to estimate the ratio between PneKC with PneA.

GTPase assay with varying amounts of PneA

Typically, the maximum ratio of PneKC monomer to PneA we could achieve was between 1:1 to 1:1.5 when using conventionally purified PneA. However, in the assay used to confirm PneA-stimulated GTPase

activity with varying amounts of PneA, the low yield and concentration of purified PneA obtained through urea denaturation and refolding became a problem. To overcome this limitation and obtain the higher amounts of PneA used in Fig. 2c, we further concentrated PneA by using a further affinity-purification step. In brief, we employed affinity purification using the His tag on PneA with Ni-NTA resin, following a similar method described for the purification of PneKC. The beads with bound PneA were washed with buffer containing 20 mM imidazole, and the protein was eluted with 200 mM imidazole. Since PneA is small, we did not dialyze the concentrated PneA against buffer without imidazole. Thus, for this assay, each reaction system contained approximately ~60 mM imidazole. The results therefore showed about 25% lower GTPase hydrolysis activity compared to assays using the same amount of PneKC with a similar amount of PneA performed in the absence of imidazole.

Nucleotide hydrolysis assay with varying amounts of GTP and ATP

We consistently observed the presence of PneA bound to purified PneKC at a similar ratio. To avoid the urea-denaturation purification process required for isolating PneA, for our Michaelis-Menten kinetics study of PneA on substrate GTP and ATP, we co-expressed the PneKC/PneA complex with an N-terminal His tag only on PneKC. The purification protocol was the same as the one described for PneKC. Quantification of this complex involved assessing the relative ratio using SDS-PAGE band pixel density measurements. Consistent with our previous co-expression experiments, the ratio of PneKC monomer to PneA was approximately 1:1. Subsequently, the purified complex was directly utilized for GTPase and ATPase assays as described for the nucleotide hydrolysis assays involving varying concentrations of GTP and ATP as substrates. The resulting data were plotted to derive Michaelis-Menten kinetic parameters.

Determination of thermal stability by differential scanning fluorimetry (DSF)

DSF experiments were performed using the CFX384 Touch Real-Time PCR Detection System from BIO-RAD, following the SYBR green melting protocol to obtain Tm values[54]. Briefly, 10-μL reaction mixture containing wild-type PneKC dimer or H35A mutant PneKC monomer at 10 μM and 10× SYPRO Orange (Sigma-Aldrich) was placed into a single well of a 384-well PCR plate. A temperature scan was performed between 12–90 °C with a 1° increment per minute. Upon completion, the obtained thermal unfolding curves were displayed as the first derivatives (dF/dT) by the RT-PCR software Bio-Rad CFX Manager 3.0.

Cryo-electron microscopy sample preparation and data collection for the "fully bound" state of PneKC

To prepare the fully bound sample for cryo-EM imaging, PneKC co-expressed with PneA was incubated with 1 mM GTPγS and $MgCl_2$. After a 5-min incubation at room temperature, 3.5 μl of the protein sample at a concentration of 1.5 mg/ml were applied to a glow-discharged Quantifoil holey carbon grid (R1.2/1.3, 400 mesh). Grids were blotted for 3.5 seconds at 100% relative humidity before being plunge-frozen in liquid ethane cooled by liquid nitrogen using the ThermoFisher Vitrobot System. Cryo-EM data were collected on a Titan Krios electron microscope (Thermo Fisher Scientific), equipped with a K3 Summit direct electron detector (Gatan) and a GIF Quantum energy filter. All cryo-EM movies were recorded in counting mode with SerialEM4[55] with the slit width of the energy filter set to 20 eV. Movies were acquired at a nominal magnification of 105,000x, corresponding to a calibrated pixel size of 0.858 Å on the specimen level. The exposure time for each movie was 6 seconds, resulting in a total dose of 65.2 electrons per $Å^2$, fractionated into 48 frames. Data collection parameters are listed in Table 1.

Table 1 | Cryo-EM data collection, refinement and validation statistics

	Fully recognized PneKC (EMD-37514) (PDB 8WGO)	Pre-binding PneKC (EMD-37337) (PDB 8W7A)	LP-bound PneKC (EMD-37339) (PDB 8W7J)
Data collection and processing			
Magnification	105 k	105 k	
Voltage (kV)	300	300	
Electron exposure (e–/$Å^2$)	65.2	50	
Defocus range (μm)	−1.0 to −2.0	−1.0 to −2.0	
Pixel size (Å)	0.858	0.858	
Symmetry imposed	C1	C1	
Initial particle images (no.)	1,301,086	1,272,986	
Final particle images (no.)	133,078	179,941	143,154
Map resolution (Å)	3.70	3.77	3.98
FSC threshold	0.143	0.143	0.143
Refinement			
Initial model used (PDB code)	AlphaFold2	8WGO	8WGO
Model resolution (Å)	4.0	4.2	4.3
FSC threshold	0.5	0.5	0.5
Map sharpening *B* factor ($Å^2$)	−187	−158.5	−182.1
Model composition			
Non-hydrogen atoms	14,375	13,017	13,481
Protein residues	1753	1586	1641
Nucleotide residues	0	0	0
Ligands	4	1	3
B factors (mean, $Å^2$)			
Protein	100.30	79.71	125.60
Nucleotide	n.a.	n.a.	n.a.
Ligand	125.39	107.78	124.46
R.m.s deviations			
Bond lengths (Å)	0.003	0.007	0.017
Bond angles (°)	0.662	1.115	1.652
Validation			
MolProbity score	1.94	1.89	1.93
Clashscore	7.19	5.54	6.24
Poor rotamers (%)	0.19	0.00	0.14
Ramachandran plot			
Favored (%)	90.30	88.37	88.41
Allowed (%)	9.35	10.67	11.10
Disallowed (%)	0.34	0.976	0.50

Cryo-electron microscopy sample preparation and data collection for PneKC under continuous peptide modification conditions

Apo PneKC was incubated with recombinantly expressed PneA at a molar enzyme: substrate ratio of 1:3 in the presence of 1 mM GTP and $MgCl_2$. After a 5-min incubation at room temperature, 3.5 μl of the protein sample at a concentration of 1.5 mg/ml were applied to a glow-discharged Quantifoil holey carbon grid (R1.2/1.3, 400 mesh). Grids were blotted for 3.5 seconds at 100% relative humidity before being plunge-frozen in liquid ethane cooled by liquid nitrogen using the ThermoFisher Vitrobot System. Cryo-EM data were collected on a

Titan Krios electron microscope (Thermo Fisher Scientific), equipped with a K3 Summit direct electron detector (Gatan) and a GIF Quantum energy filter. All cryo-EM movies were recorded in counting mode with SerialEM4[55] with the slit width of the energy filter set to 20 eV. Movies were acquired at a nominal magnification of ×105,000, corresponding to a calibrated pixel size of 0.858 Å on the specimen level. The exposure time for each movie was 6 seconds, resulting in a total dose of 50 electrons per Å^2, fractionated into 48 frames. Data collection parameters are listed in Table 1.

Cryo-electron microscopy data processing

All datasets were processed with CryoSPARC[56]. After patch motion correction was performed on the dose-fractionated movies, all frames were summed using a dose-weighting scheme to correct for radiation damage. The summed images were used for subsequent image processing except to determine the defocus values, which were estimated using patch CTF estimation on images that were summed without dose weighting. Particles were picked using blob picker followed by picking using template matching. Two- and three-dimensional (2D and 3D) classifications were performed on the selected particles, using which an initial 3D model could be reconstructed using "Ab-initial Reconstruction". The initial model was then put through a series of "Heterogeneous Refinement" to eliminate noise which may lower the final resolution. After the dataset is sufficiently homogeneous, "Homogenous Refinement" and "Non-Uniform Refinement" was performed[57]. The final resolutions were estimated based on the gold-standard criterion of Fourier shell correlation (FSC) = 0.143. The detailed workflow of the image analysis process is shown in Supplementary Fig. 4 and Supplementary Fig. 12.

Model building and refinement

The initial model of PneKC was generated with AlphaFold2[58,59]. This model showed PneKC in the monomeric form, which was duplicated and rigid-body fitted into the cryo-EM map using UCSF ChimeraX[60,61]. Model fitting was then performed manually using Coot[62], and the resulting model was then refined using real-space refinement in Phenix[63]. GTP and PneA, which were not present in the initial model but observed in the density maps, were manually added taking into account the interacting residues on the PneKC model. Iterative real-space refinement was then performed using Phenix to improve the accuracy of the model and to generate the final model, which was then verified using Ramachandran plot, MolProbity scores, and Clash scores in Phenix.

We utilized AlphaFold2-Multimer to corroborate the assembly of our PneKC dimer and the interaction between PneKC and PneA. The predicted model closely resembled our experimental dimer structure, with the interaction between PneKC and PneA, particularly in the LP region containing the first 1–15 residues, showing nearly identical configurations.

LC-TOF-MS characterization to distinguish between modified and unmodified PneA

To assess peptide modification activity, we used S-methyl methanethiosulfonate (MMTS) crosslinking[42] to assess whether PneA was modified or not. Specifically, unmodified PneA contains free cysteines that can be crosslinked to MMTS, whereas modified PneA cannot be crosslinked. The addition of mass was detected by MS analysis.

For MMTS crosslinking, PneA was incubated with 1 mM GTP, 1 mM $MgCl_2$, and 5 mM TCEP. After a 1 h incubation at room temperature in the presence or absence of 0.5 mg/ml PneKC, 10 mM MMTS was added to each sample and incubated for an additional hour at room temperature. Four samples were examined: 1) non-alkylated and 2) alkylated His_7-tagged PneA incubated without PneKC, 3) non-alkylated and 4) alkylated His_7-tagged PneA incubated with PneKC. One reaction was performed for each sample with no replicates ($n = 1$). The samples were analyzed using an Acquity Premier Protein BEH C4 column (1.7 µm, 2.1 mm × 50 mm) with a water: acetonitrile: formic acid (FA) solvent system consisting of 0.1% FA in water (solvent A) and 0.1% FA in acetonitrile (solvent B). Following injection of 10 µl sample, separation was achieved at a flow rate of 0.3 ml/min using a linear gradient of 10–90% solvent B over 8 min. The eluent from the column was directed to a SCIEX TripleTOF 5600 with DuoSpray Ion Source and detected under the following source settings: GS1 50, GS2 50, CUR 30, TEM 500, ISVF 5000, CE 10, DP 80. TOF mass spectra spanning the m/z range of 400 - 2500 m/z were collected with a 1-sec accumulation time. Deconvolution was done using the Biotool Kit in SCIEX OS Analytics, for an output range of 2000–120000 Da.

In-gel digestion for fragmented MS analysis

Protein bands were excised from freshly CCB-stained gels and plated in a 96-well microtiter plate. Excised slices were first destained twice with 200 µl of 50 mM NH_4HCO_3 and 50% acetonitrile and then dried twice with 200 µl acetonitrile. The gel pieces were rehydrated in 10 mM dithiothreitol and incubated for 60 min at 56 °C. The gel pieces were again dehydrated in 100% acetonitrile and rehydrated with 55 mM iodoacetamide in the dark for 45 min. The dried gels pieces were then incubated for 20 min in ice-cold digestion solution (12.5 ng/µl trypsin and 20 mM NH_4HCO_3) and transferred into a 37 °C incubator for digestion overnight. Finally, peptides in the supernatant were collected after being extracted twice with 200 µl extract solution (5% formic acid in 50% acetonitrile). The peptide solution was dried under nitrogen gas.

Nano-HPLC-MS/MS analysis

The peptides were separated by nanoLC using solvents A (H_2O + 0.1% FA) and B (acetonitrile + 0.1% FA) and analyzed by on-line electrospray tandem mass spectrometry. The experiments were performed on an EASY-nLC 1200 UPLC system connected to an Orbitrap Exploris 480 mass spectrometer (Thermo Fisher Scientific) equipped with an online nano-electrospray ion source. 5 µl of the peptide sample were loaded onto the trap column (Thermo Scientific Acclaim PepMap C18, 100 µm x 2 cm), with a flow of 10 µl/min for 3 min and subsequently separated on the analytical column (Acclaim PepMap C18, 75 µm x 50 cm) with a linear gradient from 5% to 35% solvent B over 58 min, 35% to 50% over 6 min and 50% to 100% over 1 min, then maintaining solvent B at 100% for another 5 min. The column was re-equilibrated at the initial conditions for 10 min. The column flow rate was maintained at 300 nl/min and the column temperature was maintained at 60 °C. An electrospray voltage of 2.3 kV was applied at the mass spectrometer inlet. The Orbitrap Exploris 480 mass spectrometer operated in data-dependent mode, automatically switching between MS and MS/MS acquisition. Survey full-scan MS spectra (m/z 350-1600) were acquired with a mass resolution of 60,000, followed by fifteen sequential high-energy collisional dissociation (HCD) MS/MS scans with a resolution of 15,000. For MS scans, the AGC target was set to 1,000,000, with a maximum injection time of 50 ms.

In the case of MS/MS analysis, the following parameters were applied: An intensity threshold of 13,000 was utilized, alongside a maximum injection time of 50 ms, while the AGC target was set to 100,000. In all experiments, a single microscan was recorded, with dynamic exclusion in place for 30 seconds. The MS/MS fixed first mass was established at 110 m/z, and a normalized collision energy (NCE) of 30% was chosen for high-energy collisional dissociation (HCD).

Database search for fragmented MS analysis

Tandem mass spectra were extracted using the Proteome Discoverer software (Thermo Fisher Scientific, version 2.4). Tandem mass spectra were searched against the Swissprot target protein database assuming trypsin as the digestion enzyme. Mass error was set to 10 ppm for precursor ions and 0.02 Da for fragment ions. Oxidation of methionine

and phosphorylation and dehydration of serine were specified as potential modifications. We specified a maximum of two allowed missed cleavage sites. The acceptance criteria for identifications included ensuring that the false discovery rate (FDR) remained below 1% for both peptides and proteins.

Reporting summary

Further information on research design is available in the Nature Portfolio Reporting Summary linked to this article.

Data availability

The three cryo-EM density maps of PneKC in the presence and absence of bound PneA or nucleotide have been deposited in the Electron Microscopy Data Bank [https://www.ebi.ac.uk/emdb/] under accession codes EMD-37337 (GTP-bound PneKC, pre-binding state), EMD-37339 (PneA (LP)-bound PneKC in the presence of GTP, LP-bound state), and EMD-37514 (PneA-bound PneKC in the presence of GTPγS, fully-recognized state). The atomic coordinates of the structures have been deposited in the Protein Data Bank [https://www.rcsb.org/] with accession codes 8W7A, 8W7J and 8WGO, respectively. Mass spectrometry data have been submitted to the iProX [https://www.iprox.cn/] database under the following iProX IDs. Fragmented MS: PXD047786 (Subproject ID for PneA incubated with PneKC^{R224A} IPX0007738002; PneA incubated with PneKC^{H61F}: IPX0007738003; PneA incubated with PneK^{C522A}: IPX0007738004; PneA incubated with PneKC^{K88A}: IPX0007738005.) Intact MS: PXD050940 (Subproject ID for PneA: IPX0008439001; Subproject ID for PneA+MMTS: IPX0008439004; Subproject ID for PneA incubated with PneKC and MMTS: IPX0008439005; Subproject ID for PneA incubated with PneKC and MMTS: IPX0008439006). Source data are provided as a Source Data file. Source data are provided with this paper.

References

1. Dang, T. & Sussmuth, R. D. Bioactive peptide natural products as lead structures for medicinal use. *Acc. Chem. Res* **50**, 1566–1576 (2017).
2. van Staden, A. D. P., van Zyl, W. F., Trindade, M., Dicks, L. M. T. & Smith, C. Therapeutic application of lantibiotics and other lanthipeptides: old and new findings. *Appl Environ. Microbiol* **87**, e0018621 (2021).
3. Vilas Boas, L. C. P., Campos, M. L., Berlanda, R. L. A., de Carvalho Neves, N. & Franco, O. L. Antiviral peptides as promising therapeutic drugs. *Cell Mol. Life Sci.* **76**, 3525–3542 (2019).
4. Agarwal, G. & Gabrani, R. Antiviral peptides: identification and validation. *Int J. Pept. Res Ther.* **27**, 149–168 (2021).
5. Roby, K. D. & Nardo, A. D. Innate immunity and the role of the antimicrobial peptide cathelicidin in inflammatory skin disease. *Drug Discov. Today Dis. Mech.* **10**, e79–e82 (2013).
6. Brice, D. C. & Diamond, G. Antiviral activities of human host defense peptides. *Curr. Med Chem.* **27**, 1420–1443 (2020).
7. Ganz, T. Defensins: antimicrobial peptides of innate immunity. *Nat. Rev. Immunol.* **3**, 710–720 (2003).
8. Kosciuczuk, E. M. et al. Cathelicidins: family of antimicrobial peptides. A review. *Mol. Biol. Rep.* **39**, 10957–10970 (2012).
9. Tan, Z. X. et al. Role of defensins in diabetic wound healing. *World J. Diab.* **13**, 962–971 (2022).
10. van Harten, R. M., van Woudenbergh, E., van Dijk, A. & Haagsman, H. P. Cathelicidins: immunomodulatory antimicrobials. *Vaccines (Basel)* **6**, 63(2018).
11. Li, C. et al. Mining and biosynthesis of bioactive lanthipeptides from microorganisms. *Front Bioeng. Biotechnol.* **9**, 692466 (2021).
12. Repka, L. M., Chekan, J. R., Nair, S. K. & van der Donk, W. A. Mechanistic understanding of lanthipeptide biosynthetic enzymes. *Chem. Rev.* **117**, 5457–5520 (2017).
13. Jungmann, N. A., Krawczyk, B., Tietzmann, M., Ensle, P. & Sussmuth, R. D. Dissecting reactions of nonlinear precursor peptide processing of the class III lanthipeptide curvopeptin. *J. Am. Chem. Soc.* **136**, 15222–15228 (2014).
14. Krawczyk, B., Voller, G. H., Voller, J., Ensle, P. & Sussmuth, R. D. Curvopeptin: a new lanthionine-containing class III lantibiotic and its co-substrate promiscuous synthetase. *Chembiochem* **13**, 2065–2071 (2012).
15. Arnison, P. G. et al. Ribosomally synthesized and post-translationally modified peptide natural products: overview and recommendations for a universal nomenclature. *Nat. Prod. Rep.* **30**, 108–160 (2013).
16. Burkhart, B. J., Hudson, G. A., Dunbar, K. L. & Mitchell, D. A. A prevalent peptide-binding domain guides ribosomal natural product biosynthesis. *Nat. Chem. Biol.* **11**, 564–570 (2015).
17. Lagedroste, M., Smits, S. H. J. & Schmitt, L. Importance of the leader peptide sequence on the lanthipeptide secretion level. *FEBS J.* **288**, 4348–4363 (2021).
18. Thibodeaux, C. J. The conformationally dynamic structural biology of lanthipeptide biosynthesis. *Curr. Opin. Struct. Biol.* **81**, 102644 (2023).
19. Lagedroste, M., Reiners, J., Knospe, C. V., Smits, S. H. J. & Schmitt, L. A structural view on the maturation of lanthipeptides. *Front Microbiol* **11**, 1183 (2020).
20. Zhang, Q., Yu, Y., Velasquez, J. E. & van der Donk, W. A. Evolution of lanthipeptide synthetases. *Proc. Natl Acad. Sci. USA* **109**, 18361–18366 (2012).
21. Ortega, M. A. et al. Structure and mechanism of the tRNA-dependent lantibiotic dehydratase NisB. *Nature* **517**, 509–512 (2015).
22. van der Donk, W. A. & Nair, S. K. Structure and mechanism of lanthipeptide biosynthetic enzymes. *Curr. Opin. Struct. Biol.* **29**, 58–66 (2014).
23. Li, B. et al. Structure and mechanism of the lantibiotic cyclase involved in nisin biosynthesis. *Science* **311**, 1464 (2006).
24. Dong, S. H. et al. The enterococcal cytolysin synthetase has an unanticipated lipid kinase fold. *Elife* **4**, e07607 (2015).
25. Rahman, I. R. et al. Substrate recognition by the class II lanthipeptide synthetase HalM2. *ACS Chem. Biol.* **15**, 1473–1486 (2020).
26. Sigurdsson, A. et al. Discovery of the lanthipeptide curvocidin and structural insights into its trifunctional synthetase CuvL. *Angew. Chem. Int Ed. Engl.* **62**, e202302490 (2023).
27. Hernandez Garcia, A. & Nair, S. K. Structure and function of a class III metal-independent lanthipeptide synthetase. *ACS Cent Sci.* **9**, 1944–1956 (2023).
28. Xu, M. et al. Functional genome mining reveals a class v lanthipeptide containing a d-amino acid introduced by an F(420) H(2) -dependent reductase. *Angew. Chem. Int Ed. Engl.* **59**, 18029–18035 (2020).
29. Liang, H., Lopez, I. J., Sanchez-Hidalgo, M., Genilloud, O. & van der Donk, W. A. Mechanistic studies on dehydration in class V lanthipeptides. *ACS Chem. Biol.* **17**, 2519–2527 (2022).
30. Wang, H. & van der Donk, W. A. Biosynthesis of the class III lantipeptide catenulipeptin. *ACS Chem. Biol.* **7**, 1529–1535 (2012).
31. Ren, H., Shi, C., Bothwell, I. R., van der Donk, W. A. & Zhao, H. Discovery and characterization of a class IV lanthipeptide with a nonoverlapping ring pattern. *ACS Chem. Biol.* **15**, 1642–1649 (2020).
32. Huang, S. et al. Discovery of a unique structural motif in lanthipeptide synthetases for substrate binding and interdomain interactions. *Angew. Chem. Int Ed. Engl.* **61**, e202211382 (2022).
33. Hernandez Garcia, A. & Nair, S. K. Structure and function of a class iii metal-independent lanthipeptide synthetase. *ACS Cent. Sci.* **9**, 1944–1956 (2023).

34. Wiebach, V. et al. An amphipathic alpha-helix guides maturation of the ribosomally-synthesized lipolanthines. *Angew. Chem. Int Ed. Engl.* **59**, 16777–16785 (2020).
35. Jungmann, N. A., van Herwerden, E. F., Hugelland, M. & Sussmuth, R. D. The supersized class iii lanthipeptide stackepeptin displays motif multiplication in the core peptide. *ACS Chem. Biol.* **11**, 69–76 (2016).
36. Grigoreva, A. et al. Identification and characterization of andalusicin: N-terminally dimethylated class III lantibiotic from Bacillus thuringiensis sv. andalousiensis. *iScience* **24**, 102480 (2021).
37. Castro, I. et al. The lanthipeptide biosynthetic clusters of the domain Archaea. *Microbiol Res* **253**, 126884 (2021).
38. Gebhard, S. A. B. C. transporters of antimicrobial peptides in Firmicutes bacteria - phylogeny, function and regulation. *Mol. Microbiol* **86**, 1295–1317 (2012).
39. Muller, W. M., Schmiederer, T., Ensle, P. & Sussmuth, R. D. In vitro biosynthesis of the prepeptide of type-III lantibiotic labyrinthopeptin A2 including formation of a C-C bond as a post-translational modification. *Angew. Chem. Int Ed. Engl.* **49**, 2436–2440 (2010).
40. Wiebach, V. et al. The anti-staphylococcal lipolanthines are ribosomally synthesized lipopeptides. *Nat. Chem. Biol.* **14**, 652–654 (2018).
41. Voller, G. H. et al. Characterization of new class III lantibiotics-erythreapeptin, avermipeptin and griseopeptin from Saccharopolyspora erythraea, Streptomyces avermitilis and Streptomyces griseus demonstrates stepwise N-terminal leader processing. *Chembiochem* **13**, 1174–1183 (2012).
42. Lee, H., Wu, C., Desormeaux, E. K., Sarksian, R. & van der Donk, W. A. Improved production of class I lanthipeptides in Escherichia coli. *Chem. Sci.* **14**, 2537–2546 (2023).
43. Evans, R. et al. Protein complex prediction with alphafold-multimer. Preprint at *BioRxiv* 2021.10.04.463034 (2021).
44. Hegemann, J. D. & Sussmuth, R. D. Matters of class: coming of age of class III and IV lanthipeptides. *RSC Chem. Biol.* **1**, 110–127 (2020).
45. Julian D. Hegemann†, L.S., ||, Michael L. Gross‡,*, and Wilfred A. van der Donk. Mechanistic Studies of the Kinase Domains of Class IV Lanthipeptide Synthetases. *ACS Chem Biol*. **14**, 1583–1592 (2020).
46. Chen, L. et al. Structural basis for the catalytic mechanism of phosphothreonine lyase. *Nat. Struct. Mol. Biol.* **15**, 101–102 (2008).
47. Goto, Y., Okesli, A. & van der Donk, W. A. Mechanistic studies of Ser/Thr dehydration catalyzed by a member of the LanL lanthionine synthetase family. *Biochemistry* **50**, 891–898 (2011).
48. Krissinel, E. & Henrick, K. Inference of macromolecular assemblies from crystalline state. *J. Mol. Biol.* **372**, 774–797 (2007).
49. Julie D.Thompson, D.G.H.a.T.J.G. CLUSTAL W: improving the sensitivity of progressive multiple sequence alignment through sequence weighting, position-specific gap penalties and weight matrix choice. *Nucleic Acids Res.* **22**, 4673–80 (1994).
50. Walker, M. C. et al. Precursor peptide-targeted mining of more than one hundred thousand genomes expands the lanthipeptide natural product family. *BMC Genomics* **21**, 387 (2020).
51. Larkin, M. A. et al. Clustal W and clustal X version 2.0. *Bioinformatics* **23**, 2947–2948 (2007).
52. Robert, X. & Gouet, P. Deciphering key features in protein structures with the new ENDscript server. *Nucleic Acids Res* **42**, W320–W324 (2014).
53. Xu, X. et al. Mechanistic insights into the regulation of cell wall hydrolysis by FtsEX and EnvC at the bacterial division site. *Proc. Natl Acad. Sci. USA* **120**, e2301897120 (2023).
54. Dang, M., Li, Y. & Song, J. Tethering-induced destabilization and ATP-binding for tandem RRM domains of ALS-causing TDP-43 and hnRNPA1. *Sci. Rep.* **11**, 1034 (2021).
55. Mastronarde, D. N. Automated electron microscope tomography using robust prediction of specimen movements. *J. Struct. Biol.* **152**, 36–51 (2005).
56. Punjani, A., Rubinstein, J. L., Fleet, D. J. & Brubaker, M. A. cryoSPARC: algorithms for rapid unsupervised cryo-EM structure determination. *Nat. Methods* **14**, 290–296 (2017).
57. Punjani, A., Zhang, H. & Fleet, D. J. Non-uniform refinement: adaptive regularization improves single-particle cryo-EM reconstruction. *Nat. Methods* **17**, 1214–1221 (2020).
58. Jumper, J. et al. Highly accurate protein structure prediction with AlphaFold. *Nature* **596**, 583–589 (2021).
59. Mirdita, M. et al. ColabFold - Making protein folding accessible to all. *Nat Methods* **6**, 679–682 (2022).
60. Pettersen, E. F. et al. UCSF ChimeraX: structure visualization for researchers, educators, and developers. *Protein Sci.* **30**, 70–82 (2020).
61. Goddard, T. D. et al. UCSF ChimeraX: meeting modern challenges in visualization and analysis. *Protein Sci.* **27**, 14–25 (2018).
62. Emsley, P., Lohkamp, B., Scott, W. G. & Cowtan, K. Features and development of Coot. *Acta Crystallogr D. Biol. Crystallogr* **66**, 486–501 (2010).
63. Liebschner, D. et al. Macromolecular structure determination using X-rays, neutrons and electrons: recent developments in Phenix. *Acta Crystallogr D. Struct. Biol.* **75**, 861–877 (2019).

Acknowledgements

We are grateful to Adam Yuan at the Department of Biological Sciences, National University of Singapore for reagents. We thank the staff at cryo-EM Center of the National University of Singapore, for their help in data collection. We thank the Protein and Proteomics Center (PPC) at the National University of Singapore for conducting the intact mass spectrometry experiments. We thank the Luo lab members for helpful discussion and comments on the project. This work was supported by a Start-up grant from the National University of Singapore, three Ministry of Education Tier 2 Grants (MOE-T2EP30222-0015, T2EP30223-0029 & T2EP30123-0017), and a National Research Foundation grant (NRF-CRP22-2019-0001) to M. L., and a Singapore Academies South-East Asia Fellowship to B.K.G.

Author contributions

M.L. conceived the project, designed and supervised research, analyzed data, and wrote the paper with help from Y.F.L.; Y.F.L. performed all biochemical reconstitutions, functional characterizations, EM data collection, and model building with help from K.S.; Z.X.L. and Y.B.X. performed the fragmented mass spectrometry analysis; K.F.Z. and B.K.G contributed to enzymatic assays; J.S. helped with EM data collection.

Competing interests

The authors declare no competing interests.

Additional information

Supplementary information The online version contains supplementary material available at https://doi.org/10.1038/s41467-024-51600-6.

Correspondence and requests for materials should be addressed to Min Luo.

Peer review information *Nature Communications* thanks Jorge López-Alonso and the other, anonymous, reviewers for their contribution to the peer review of this work. A peer review file is available.